LEVEL

Semiannual Technical Summary

Seismic Discrimination

30 September 1978

Lincoln Laboratory

MASSACHUSETTS INSTITUTE OF TECHNOLOGY

LEXINGTON, MASSACHUSETTS
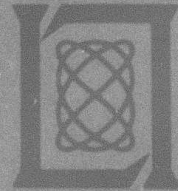
79 03 12 117

This report may be reproduced to satisfy needs of U.S. Government agencies.

The views and conclusions contained in this document are those of the contractor and should not be interpreted as necessarily representing the official policies, either expressed or implied, of the United States Government.

This technical report has been reviewed and is approved for publication.

FOR THE COMMANDER

Raymond L. Loiselle, Lt. Col., USAF
Chief, ESD Lincoln Laboratory Project Office

MASSACHUSETTS INSTITUTE OF TECHNOLOGY

LINCOLN LABORATORY

SEISMIC DISCRIMINATION

SEMIANNUAL TECHNICAL SUMMARY REPORT
TO THE
DEFENSE ADVANCED RESEARCH PROJECTS AGENCY

1 APRIL – 30 SEPTEMBER 1978

ISSUED 23 JANUARY 1979

LEXINGTON   MASSACHUSETTS

ABSTRACT

This report describes 20 investigations in the fields of seismic discrimination and the analysis of data from a global seismic network. These are grouped as follows: the estimation of event location and focal depth (4 contributions), the estimation of the source moment tensor (5 contributions), miscellaneous studies (6 contributions), and computer systems and data collection (5 contributions).

CONTENTS

SUMMARY

This is the twenty-ninth Semiannual Technical Summary report describing the activities of Lincoln Laboratory funded under Project Vela Uniform. This report covers the period 1 April to 30 September 1978. Project Vela Uniform is a program of research into the discrimination between earthquakes and nuclear explosions by seismic means. A recent new emphasis of the project is in the development of the data-handling and analysis techniques that might be appropriate for the monitoring of a potential Comprehensive Test Ban Treaty, presently under negotiation. The objectives of the Lincoln Laboratory program are to carry out fundamental research with the seismological problems associated with the detection, location, and identification of earthquakes and nuclear explosions, and to develop both processing algorithms and data-management-system techniques that may be implemented as part of U.S. activities associated with an international treaty monitoring network. Much of this research involves the analysis of digital seismic data from the new network of high-quality seismic stations called Seismic Research Observatories (SROs).

A fundamental problem in seismic-data analysis is the development of rapid automated or semiautomated methods for the routine estimation of source location and focal depth, and the association of long-period (LP) data with events determined from short-period (SP) arrivals. One investigation describes an attempt to determine source azimuth and distance directly from surface-wave data, for comparison with SP data. With further refinement, this technique may greatly assist the association problem. Event location is primarily a problem in path calibration, and two studies address the application of the master-event technique. If local crustal structure is relatively simple and well known, it is shown that the addition of regional data, using travel times of crustal phases, can provide a noticeable improvement to the quality of epicenters determined from teleseismic data alone. The master-event technique can also be useful in the estimation of the relative focal depth of events. In another study, the application of seismic ray tracing to event location in a complex area is described.

We have begun a series of investigations into methods for the estimation of fault plane solutions and the moment tensor. Two studies investigate the direct inversion of body-wave amplitudes to obtain the moment tensor. In the first, a case is described in which inversion leads to a predominantly double-couple source which has an orientation rather more consistent with the tectonic environment than the published fault plane solution. The second study attempts to estimate the potential errors introduced into the moment tensor inversion by structural inhomogeneity. Improvements to the determination of fault plane solutions depend critically on the development of nonsubjective approaches. One such approach, using a linear-estimation procedure, is described. Another study outlines the possible utilization of synthetic seismograms computed by the superposition of normal modes, and formulates the inverse problem of estimating the moment tensor from observed seismograms.

A number of miscellaneous studies are included, consisting mainly of analysis of SRO data. Two investigations have focused on the problem of event-detection algorithms. The first assesses the performance of the current SRO event detector, and demonstrates a high incidence of false alarms and disappointing performance at some stations. The second discusses some potential improvements to detection algorithms. Another study has begun to assess the usefulness of digital waveforms in the estimation of body-wave magnitude m_b. Station amplitude bias

vii

appears to be a significant effect, and calibration by source region may be possible. A study of mantle Love-wave dispersion is a beginning of a global analysis of regional variations in phase velocity and Q. Rayleigh-wave dispersion is used to estimate the structure of the lithosphere in a remote aseismic area of the South Atlantic. Investigations of the propagation of the crustal phase Lg continue. A study shows that the observed phase velocities of the vertical component of Lg are consistent with the expected behavior of higher-mode Rayleigh waves.

We continue to make improvements to our in-house computer system, and are focusing our programming effort into those areas that will have eventual application in a global treaty monitoring context. A new version of our Data Analysis and Display System (DADS) is described, together with improvements in our waveform graphics package and the speed of display of waveforms on our storage display terminals. We are currently retrieving SRO data from the Data-computer, and software developments in this area are described. We are reducing the size of our library collection of digital seismic data so that proper tape maintenance can be instituted.

M. A. Chinnery

I. ESTIMATION OF EVENT LOCATION AND FOCAL DEPTH

A. AUTOMATIC EVENT LOCATION USING 3-COMPONENT SURFACE-WAVE DATA

The association of surface-wave trains with a specific event, particularly when successive surface-wave trains overlap, is a complicated process. Without a reasonably accurate knowledge of the variation of group velocity across the surface of the earth, such associations are often ambiguous for mixed events. We describe here a technique for locating seismic events using 3-component surface-wave data, which may also be of use in locating events when short-period (SP) data are not available because of very high levels of SP noise such as often are observed at island stations. The method is designed to be used in conjunction with a power-based surface-wave detector, and can provide preliminary locations with a moderate degree of accuracy from surface-wave segments as short as 60 sec in duration.

Suppose we have 3-component surface-wave data in the form of vertical, north-south, and east-west seismometer orientation, denoted by $Z(t)$, $N(t)$, and $E(t)$, respectively. We apply a bandpass filter at 20 sec period to each channel, and use a power detector to determine arrivals of Rayleigh-wave Airy phases on the vertical component. If the arrival is coming from an azimuth Θ with respect to north, then radial $R(t)$ and transverse $Tr(t)$ components, given by

$$R(t) = -\cos\Theta\, N(t) - \sin\Theta\, E(t)... \qquad (I-1)$$

$$Tr(t) = +\sin\Theta\, N(t) - \cos\Theta\, E(t)... \qquad (I-2)$$

will then contain radial-component Rayleigh waves and transverse-component Love waves, respectively.

In addition, $R(t)$ and $Z(t)$ are polarized such that

$$Z(t) = i\varepsilon R(t)... \qquad (I-3)$$

where ε, the ellipticity, is a constant for a particular frequency, depending only upon structure beneath the recording station, and the factor i accounts for the 90° phase difference between radial and transverse components. If we phase shift $Z(t)$ by 90°, it will be in phase with $R(t)$. Suppose we form the cross-correlogram

$$\int_0^T R(t)\, Z^h(t)\, dt$$

of $R(t)$ with the (90° phase shifted) Hilbert transform $Z^h(t)$ of $Z(t)$ over a time window of length T, then

$$\int_0^T R(t)\, Z^h(t)\, dt = -\cos\Theta \int_0^T N(t)\, Z^h(t)\, dt - \sin\Theta \int_0^T E(t)\, Z^h(t)\, d$$

or

$$I_{RZ} = -\cos\Theta\, I_{NZ} - \sin\Theta\, I_{EZ}$$

1

will have a maximum value at the epicenter azimuth Θ, or at

$$\frac{\partial I_{RZ}}{\partial \Theta} = 0 \quad , \qquad \text{given by} \quad \Theta = \tan^{-1}\left(\frac{I_{EZ}}{I_{NZ}}\right)\ldots \quad . \tag{I-4}$$

We may thus determine azimuth Θ via Eq. (I-4) by extracting a window of length T of $Z(t)$ centered around the time given by the detector output, calculating $Z^h(t)$, and cross-correlating it with the same windows in time of $N(t)$ and $E(t)$. We may generate radial and transverse components $R(t)$ and $Tr(t)$ corresponding to $Z(t)$ through Eqs. (I-1) and (I-2). A check upon the accuracy of Θ is provided by the ratio of $R(t)/Z^h(t)$ at peak power of $Z(t)$: this, through Eq. (I-3), should be the ellipticity e, which must be greater than -1.0. Typical values of t at 20 sec period are -0.6 to -0.9. Now that we have $Tr(t)$, we can attempt to detect the Love-wave arrival corresponding to the Rayleigh wave detected by searching for maximum power of $Tr(t)$ over a window preceding the Rayleigh wave. The Rayleigh- and Love-wave arrival times T_R and T_L are given by

$$T_R = \frac{\Delta}{U_R} \quad \text{and} \quad T_L = \frac{\Delta}{U_L}$$

where Δ is the epicentral distance, and U_R and U_L are the Rayleigh- and Love-wave group velocities at 20 sec period. Now,

$$T_L - T_R = \Delta\left(\frac{1}{U_L} - \frac{1}{U_R}\right) = \Delta(S_L - S_R) = \delta\Delta S$$

where S is the slowness $1/U$. While both U_R and U_L vary considerably over different tectonic structures, their slowness difference δS is remarkably constant; in a continuation of a study of Rayleigh- and Love-wave group velocities across Eurasia,[1] δS values of 0.037 with a standard deviation of 0.004 have been obtained from a suite of several hundred events.

We have tested this technique on a suite of 3-component seismograms recorded at Mashhad SRO (MAIO) from 78 events within Eurasia at distances of 10° to 75°. The propagation paths involved are of extreme structural complexity. Tests of various window lengths T for the determination of azimuth Θ showed that windows as short as 60 sec in length provided the best results. We used $\delta S = 0.037$ sec/km for the distance determination. Figures I-1(a) and (b) show the errors in azimuth Θ and distance Δ (deviations from actual values based on PDE event locations). Also shown in Fig. 1-1 is the mislocation (c), defined as the distance between the true epicenter and that of a point at azimuth Θ and distance Δ from the station. The azimuth is determined to within 15° for 56 percent of the 79 events studied; but an alarmingly high 27 percent of the events are mislocated in azimuth by more than 30°. However, if we apply the constraint that the ellipticity e at peak power lies between -0.5 and -1.0 [satisfied for 42 (or 53 percent) of the events used], this reduces the number of such gross mislocations dramatically. The distance determination scheme works reasonably well (34 percent within 5°), and 60 percent within 15° of true distance: here again, the number of events for which $\delta\Delta$ exceeds 30° is reduced by application of the ellipticity constraint on azimuth. The mislocation statistics are not very encouraging — only 50 percent of the events are located to better than 15° in distance. These large mislocations are primarily due to errors in the azimuth determination, and an improvement of the latter is clearly required. The technique requires, however, a minimal amount of computer time and is designed to be used in conjunction with a surface-wave detection algorithm. It may

prove to be of use in a surface-wave association scheme, and we propose further investigation of its application.

<div align="right">R. G. North</div>

B. THE MASTER-EVENT METHOD FOR LOCATING EXPLOSION EPICENTERS USING CRUSTAL PHASES

This report concludes the experiment of evaluating the utility of crustal phases in locating explosion epicenters. Previously, we determined a two-layer crustal model for the Basin and Range province[2,3] within which the majority of our near-regional stations are located. Next, we relocated events Greeley, Scroll, and Rulison[3] using the Jeffreys-Bullen (J-B) travel-time tables for teleseismic arrivals and our own Basin and Range tables for crustal-phase arrivals. These relocation results showed that a large amount of data in the regional distance range was able to produce epicenters as accurate as those derived from substantial teleseismic data. Furthermore, adding observations from a few good regional stations to a teleseismic data set usually improves the resulting epicenter in both accuracy and quality. Finally, to estimate the effect of bias in the travel-time tables, we present here the results of relocating the events Rex, Boxcar, and Commodore using the master-event method. This method is, in effect, a means of automatically applying the usual station corrections.

The NTS explosion Greeley was selected as the master event because it had the best distribution of reporting stations. The corresponding travel-time residuals were then subtracted from the arrival times for the other events. The difference between the Greeley residual and the average residual of all four explosions averaged over the set of common stations had a mean of 0.68 sec, with a standard deviation of 4.9 sec. This shows that Greeley residuals are representative of all four explosions.

The results of relocating the epicenters of Rex, Boxcar, and Commodore after correcting for the Greeley residuals are listed in Tables I-1, I-2, and I-3. They show that the master-event method gives more-accurate epicenters than by using uncorrected arrivals in all three cases. The reduction in mislocation varies from approximately a factor-of-2 to a factor-of-6 and depends on the number of reporting stations. However, there does not appear to be any significant improvement in the quality of the epicenter as measured by the area of the corresponding confidence ellipse. In the case of a large well-recorded event such as Boxcar, these results show that the epicenter can be located approximately 1 km away from its known position with a confidence ellipse area of less than 8 km^2.

We wish to emphasize a general conclusion of these location experiments. Accurate epicenters (<5 km mislocation) can be derived from crustal-phase data if either station corrections are known or if the crustal structure is both simple and well determined. Of the two options, station corrections measured by observing a master event are preferable to just knowing the crustal structure. However, in an area as homogeneous and well known as the Basin and Range, epicenters accurate to within 10 km can be found without resorting to a master event. The advantage to the latter approach is that the epicenters will stay accurate over a range of source and station locations as long as they both remain within the same geologic province. Strictly speaking, station corrections measured from a master event will only apply to events in the immediate vicinity of that epicenter.

<div align="right">R. E. Needham
D. W. McCowan</div>

<div align="center">3</div>

TABLE 1-1

RESULTS OF THE REX MASTER-EVENT RELOCATION EXPERIMENT

	Latitude (°N)	Longitude (°W)	Depth (km)	Confidence Ellipse Area (km²)	Mislocation (km)	Number of Observations
Rex Hypocenter	37.27	116.43	0.672	–	–	–
All Data	37.20 ± 0.02	116.41 ± 0.02	1.0G	9.73	8.0	79
Uncorrected Greeley Common Data	37.23 ± 0.02	116.40 ± 0.02	1.0G	15.75	5.2	47
Corrected Greeley Common Data	37.24 ± 0.02	116.42 ± 0.02	1.0G	15.69	3.5	47
Corrected Greeley Common Data Res ≥ −2.0, <2.0	37.24 ± 0.02	116.45 ± 0.02	1.0G	16.73	3.8	41
Corrected Greeley Common Data Res ≥ −1.0, <1.0	37.23 ± 0.02	116.44 ± 0.03	1.0G	18.54	4.5	36
Uncorrected Greeley Common Data Delta ≤ 10.0 Pn Data Only	37.21 ± 0.03	116.44 ± 0.03	1.0G	21.32	6.7	22
Corrected Greeley Common Data Delta ≤ 10.0 Pn Data Only	37.22 ± 0.03	116.43 ± 0.03	1.0G	21.42	5.6	22

4

TABLE 1-2

RESULTS OF THE BOXCAR MASTER-EVENT RELOCATION EXPERIMENT

	Latitude (°N)	Longitude (°W)	Depth (km)	Confidence Ellipse Area (km^2)	Mislocation (km)	Number of Observations
Boxcar Hypocenter	37.30	116.46	1.16	–	–	–
All Data	37.33 ± 0.01	116.41 ± 0.01	1.0G	4.24	5.5	238
Uncorrected Greeley Common Data	37.33 ± 0.02	116.39 ± 0.02	1.0G	7.59	7.1	180
Corrected Greeley Common Data	37.29 ± 0.02	116.45 ± 0.02	1.0G	7.59	1.1	180
Corrected Greeley Common Data Res ⩾ −2.0, ⩽ 2.0	37.29 ± 0.02	116.45 ± 0.02	1.0G	7.87	1.1	165
Corrected Greeley Common Data Res ⩾ −1.0, ⩽ 1.0	37.29 ± 0.02	116.45 ± 0.02	1.0G	8.32	1.1	157
Uncorrected Greeley Common Data Delta ⩽ 10.0 Pn Data Only	37.29 ± 0.02	116.41 ± 0.02	1.0G	18.16	4.6	25
Corrected Greeley Common Data Delta ⩽ 10.0 Pn Data Only	37.30 ± 0.02	116.41 ± 0.02	1.0G	17.56	4.4	25

TABLE 1-3

RESULTS OF THE COMMODORE MASTER-EVENT RELOCATION EXPERIMENT

	Latitude (°N)	Longitude (°W)	Depth (km)	Confidence Ellipse Area (km²)	Mislocation (km)	Number of Observations
Commodore Hypocenter	37.13	116.06	0.746	–	–	–
All Data	37.18 ± 0.01	116.07 ± 0.01	1.0G	4.12	5.6	279
Uncorrected Greeley Common Data	37.18 ± 0.01	116.05 ± 0.02	1.0G	6.75	5.6	173
Corrected Greeley Common Data	37.15 ± 0.01	116.11 ± 0.02	1.0G	6.75	5.0	173
Corrected Greeley Common Data Res ≤ 2.0, > –2.0	37.14 ± 0.02	116.06 ± 0.02	1.0G	7.63	1.1	165
Corrected Greeley Common Data Res ≤ 1.0, > –1.0	37.15 ± 0.02	116.08 ± 0.02	1.0G	9.14	0.0	126
Uncorrected Greeley Common Data Delta ≤ 10.0 Pn Data Only	37.11 ± 0.03	116.04 ± 0.02	1.0G	17.07	2.8	26
Corrected Greeley Common Data Delta ≤ 10.0 Pn Data Only	37.13 ± 0.03	116.04 ± 0.02	1.0G	17.07	1.8	26

6

C. SEISMIC RAY TRACING FOR RELOCATING OCEANIC RIDGE EARTHQUAKES

The wide scatter and systematic offset of earthquake epicenters away from the narrow tectonic axis defined by the oceanic ridge crests suggests that large location errors may exist. The errors could result from the fact that oceanic ridge earthquake events are small (m_b < 5.0) and thus are only recorded by nearby stations whose azimuthal distribution is generally biased. Accordingly, for earth-structure models which have an average velocity slower than the true velocity, the location will be "pulled" along the general azimuth toward the region of the greatest number of stations. Conversely, a "fast" model would "push" the location away from the dominant stations' region. Also, azimuthal ray bending due to the shallow two-dimensional structure beneath the ridges could introduce errors.

In previous SATS,[2,3] Phillips and others have employed realistic earth velocity models of oceanic ridge structure to calculate travel-time/epicentral-distance tables. Ray-tracing methods[4] were used to account for both the higher crustal velocity and two-dimensional earth structure beneath oceanic ridges.[5] Significantly, the new ocean ridge model produced much faster travel times as compared with the spherical earth, Jeffrey-Bullen,[6] and Herrin[7] models which are generally used to locate earthquakes [i.e., International Seismological Center (ISC)].

As might be expected, the most marked travel-time difference occurred for near-surface events. Travel times were typically 4 sec faster than those computed with the J-B model over the epicentral distance range 20° to 50°. Between 50° and 70° the difference was 5 sec, and for distances less than 20° the ocean ridge model computed travel times were 6 sec faster. Notably, the dependence of travel time on the azimuth to the station relative to the ridge's trend is very small (<0.3 sec) for epicentral distances greater than 10°. Solomon and Julian[8] drew a similar conclusion in their study of azimuthal ray-bending effects on focal-plane solutions along ridges.

The effect of using a realistic, oceanic ridge velocity model for relocating mid-Atlantic ridge earthquakes was demonstrated in a previous SATS[3] for a few events (10) in a small region north of the Azores. Here, the ridge's tectonic axis is especially well defined by high-precision bathymetric and micro-earthquake surveys.[9] This work clearly showed that the use of travel-time tables derived from the faster ocean ridge earth model resulted in moving the ISC-reported locations westward, away from the dominant North American station region and much closer to the ridge's tectonic axes. In fact, by depth constraining the events to the base of the oceanic lithosphere (~110 km), most events could be moved exactly onto the ridge crest axis! However, since the maximum depth of events along the spreading axis is probably less than 10 km due to the thin lithosphere here, such a depth constraint is not reasonable. Alternatively, the same relocation effect could also be accomplished by increasing the average velocity of the ocean ridge model even more over the J-B model to provide faster travel times. An additional travel-time decrease of about 1 sec (25 percent) for the epicentral distance range of 20° to 70° for a near-surface event would approximate the 110-km depth constraint.

We have recently completed a broader test of the efficacy of the ocean ridge velocity model (ORM) for relocating earthquakes. For this work, we chose two large regions on the North and Central Atlantic ridges (Figs. I-2 and I-3) where there is pronounced systematic offset and wide scatter of the ISC earthquake epicenters relative to the well-charted ridge axes; 86 events were examined in all (42 and 44, respectively). The azimuth to the dominant recording-station region in North America for both areas is to the northwest. The relocation program of the DADS for the PDP-7 computers was used to individually process each event.

TABLE I-4

EPICENTER RELOCATION STATISTICS MID-ATLANTIC RIDGE

	Northern Region (Fig. I-2)		Central Region (Fig. I-3)		Combined Regions	
	J-B	ORM	J-B	ORM	J-B	ORM
Mean Offset Distance (km) from Ridge Axis*	12.62	10.71	15.52	9.77	14.10	10.23
Standard Deviation (S.D.)	10.30	10.21	14.83	9.12	12.83	9.62
Number of Events (N)	42		44		86	
Variance Ratio $(S.D.)^2_{J-B}/(S.D.)^2_{ORM}$	1.02		2.64		1.78	
F-Test Significance Value (95-percent Probability) for 2 (N – 1) Degrees of Freedom	1.50		1.37		1.48	
Accumulative Offset Distance (km)†	–248	–72	95	28	–	–
Offset Distance Decrease (percent)	71.0		70.6		–	

* Offset distances are measured to nearest point on ridge axis.

† Individual offset-distance measurements on the North American plate side of ridge axis (left) are taken as negative (both Figs. I-2 and I-3). Offsets measured on the European (Fig. I-2) and African (Fig. I-3) plates (right) are taken as positive.

The results of these relocations are shown by the arrows in Figs. I-2 and I-3. Note the reduced scatter and general shift of the earthquake epicenter pattern toward the ridge axis. These effects are summarized quantitatively in Table I-4 where the mean values of the offset distance for the J-B and ORM models are compared. The decrease for both regions combined is about 4 km (i.e., 14.1 vs 10.2 km) for the ORM. For the Central Atlantic epicenter, it is even more dramatic (i.e., 15.52 vs 9.8 km). Also, the change in the variance of the mean offset values is significant at the 95-percent probability for both regions.

The eastward and southward shift of each region's epicenter pattern, respectively, is demonstrated by the decrease in the accumulative offset-distance values in Table I-4. That is, if seismicity is normally distributed about the plate boundary defined by the ridge axis, as might be expected, the sum of the offset distances should be zero for a large number of events. A large accumulative distance value would suggest a systematic offset. Note that for both the J-B and ORM models, the locations are to the west and north of the plate boundary. However, in both regions the accumulative offset-distance values decrease markedly toward zero for the ORM relocated events. In fact, there has been an approximately 70-percent decrease in the accumulated offset distance (i.e., 248 vs 72 km and 95 vs 28 km, respectively). Presumably, an additional 30-percent faster travel-time decrease for the ORM over the J-B travel times would have centered the epicenter pattern over the ridge axis. Such a model would imply an additional 1-sec decrease in travel times as compared with the J-B model derived tables. This is in reasonable agreement with the 110 km depth constrained relocation effect noted earlier.

As a result of these encouraging test results, we are now developing a relocation program for the PDP-11 computers to batch process all mid-Atlantic ridge earthquake epicenters with travel-time tables derived from the new ocean ridge structure model. This work should provide a much-improved delineation of the ridge axis, especially in regions such as the South Atlantic, where little topographic information is presently available.

<div style="text-align: right">

J. D. Phillips
R. E. Needham
R. M. Sheppard

</div>

D. RELATIVE DEPTH AND SEISMIC MONITORING

It seems a reasonable proposition that all major shallow earthquakes occur below the depth of the deepest underground explosions. If this were true, then earthquake monitoring in a given region would be simplified by accurate location of each event in a region with respect to the shallowest large earthquake in the same region. Only those events significantly above the master earthquake would require special attention. Such a culling scheme is only practical in a tectonically active region such as Central Asia or along the Kuril and Kamchatka arcs. However, it is in these regions where culling is essential to make the monitoring effort manageable, given the immense quantity of incoming data.

To gain some insight into the practical difficulties of using such a scheme, two data sets were compiled from ISC arrival times stored in a computer disk file. One set was from aftershocks of an earthquake that occurred beneath the Aleutian trench (Fig. I-4) about 2 months after the Rat Island earthquake of 4 February 1965. The other set was from earthquakes in the southern part of the Kuril arc (Fig. I-5), one of the world's most active regions of shallow earthquakes in the last 15 years.

9

The relative locations were computed by a technique described in Fitch and Jackson, and Jackson and Fitch.[2] The uncertainties in relative depth are primarily controlled by the station coverage for each secondary event. Nonrandom errors in reading arrival times can significantly bias the relative location and, in particular, the relative depth of the less-well-recorded events. To some extent, this is a consequence of using a least-squares of L2 norm as a solution criterion.

The Rat Island locations, shown in vertical sections normal to the arc in Figs. I-6 and I-7, reveal activity in a zone inclined toward the north. The station distribution is grossly non-uniform, with the less-well-recorded aftershocks having no station coverage in the southern half of the focal sphere. Without arrival times from ADAK, the closest station at a distance of about 350 km toward the ENE, these locations are significantly more scattered about the master. The importance of ADAK is illustrated in Figs. I-6 and I-7. A much shallower inclination to the zone and diminished uncertainties result from a change from 56° to 95° in the takeoff angle for the ray path from the master to ADAK. This is equivalent to assuming a direct rather than a refracted first arrival at ADAK. In either case, about half the activity is above the master if the measures of uncertainty are taken as one standard deviation which is more than 20 km for the less-well-recorded aftershocks. To be useful in the context of seismic monitoring, smaller uncertainties are required — say, less than 10 km for one standard deviation.

Figure I-8 shows that the majority of the Kuril earthquakes are better located with respect to their master than are the Rat Island aftershocks. Station coverage is more complete because of the large number of Japanese stations and a significant increase in the total number of reporting stations in the 5-year interval between the times of the Rat Island and Kuril master earthquakes. In fact, one standard deviation in relative depth is less than 10 km for Kuril events located with more than 60 differential arrival times. This is illustrated in Fig. I-9. In Fig. I-8, the events with the larger uncertainties form a halo on the seaward side of the dense cluster of events that mark the contact zone between the Asian and Pacific plates. Apparently, the events in the halo have biased as well as highly uncertain locations relative to the master. These events account for 15 percent of the total number.

If station coverage improves with time, as it surely has in the 8 years since the Kuril master earthquake, the utility of a relative location scheme such as the one proposed here must also improve. The same cannot be said for earthquake locations computed with uncalibrated travel times.

<div align="right">T. J. Fitch</div>

REFERENCES

1. Seismic Discrimination SATS, Lincoln Laboratory, M.I.T. (31 March 1977), DDC AD-A045453/8.

2. Ibid. (30 September 1977), DDC AD-A050584/2.

3. Ibid. (31 March 1978), DDC AD-A057279.

4. B. R. Julian, "Ray Tracing in Arbitrarily Heterogeneous Media," Technical Note 1970-45, Lincoln Laboratory, M.I.T. (31 December 1970), DDC AD-720795.

5. L. Steinmetz, R. B. Whitmarsh, and V. S. Moreira, "Upper Mantle Structure Beneath the Mid-Atlantic Ridge North of the Azores Based on Observations of Compressional Waves," Geophys. J. R. Astr. Soc. 50, 353-380 (1977).

6. H. Jeffreys and K. E. Bullen, "Seismological Tables," British Association, Gray-Milne Trust (1940).

7. E. Herrin, "1968 Seismological Tables for P Phases," Bull. Seismol. Soc. Am. 58, 1193 (1968).

8. S. C. Solomon and B. R. Julian, "Seismic Constraints on Ocean-Ridge Mantle Structure: Anomalous Fault-Plane Solutions from First Motions," Geophys. J. R. Astr. Soc. 38, 265-285 (1974).

9. T. J. G. Francis and I. T. Porter, "Median Valley Seismology: The Mid-Atlantic Ridge Near 45°N," Geophys. J. R. Astr. Soc. 34, 279-311 (1973).
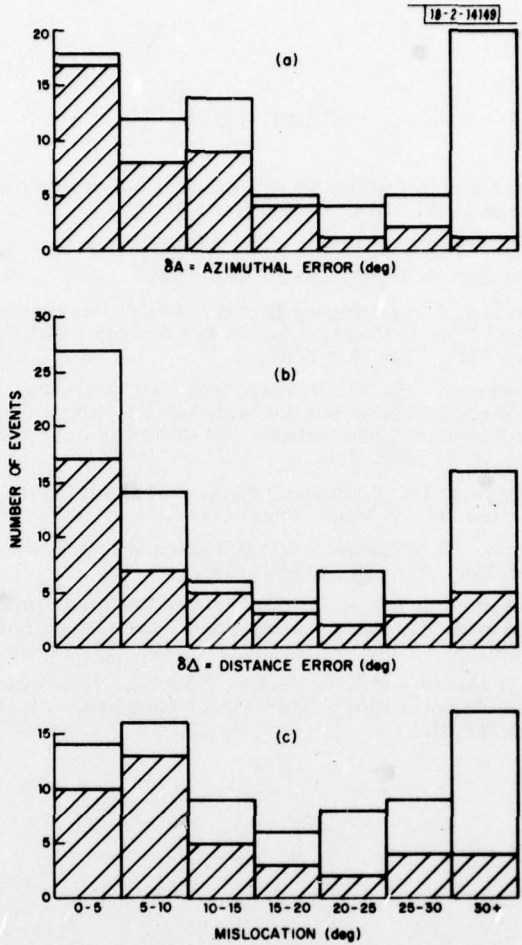
Fig. I-1. Histograms of errors in azimuth (a) and distance (b), and mislocation (c) from surface-wave location scheme described in text. Shaded portion shows results obtained with application of constraint on ellipticity value.
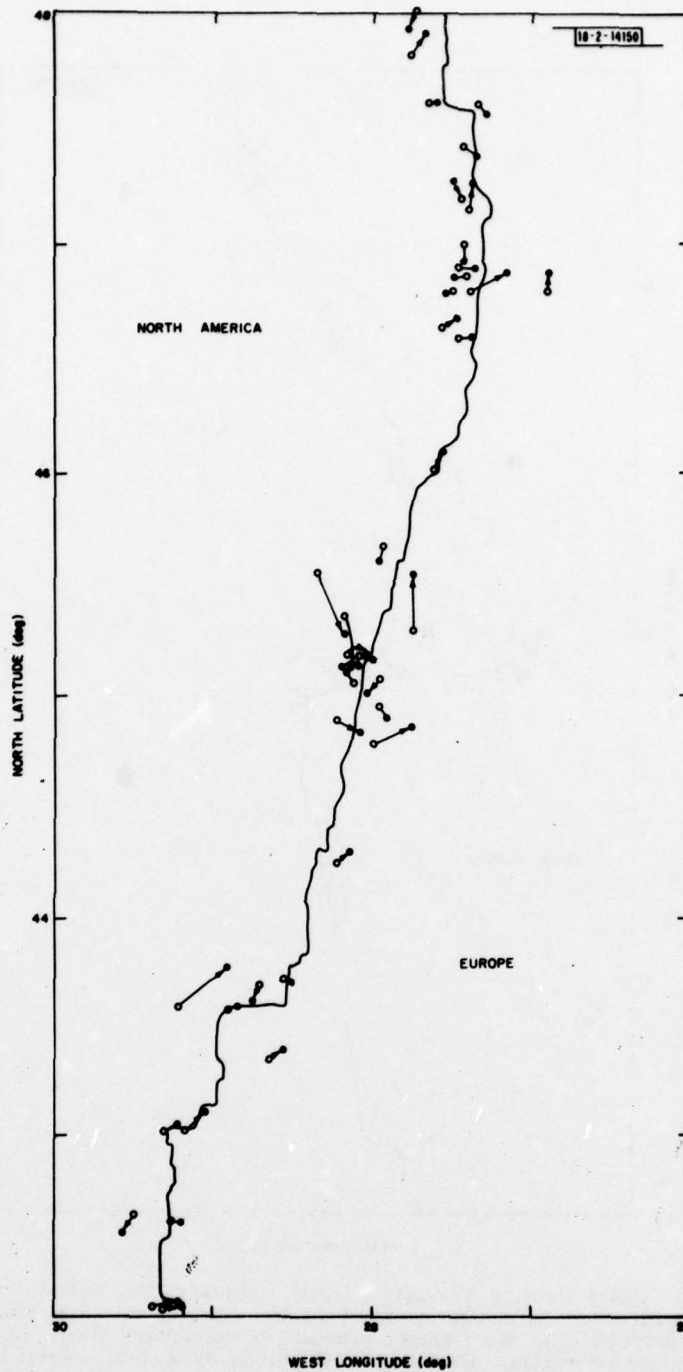
Fig. I-2. Chart showing relocation (solid circles) of ISC Bulletin epicenters (open circles) for North America and Europe using ocean ridge structure velocity model (ORM). Note closer grouping of epicenters about ridge axis for ORM relocated events. Events are for period 1964-1973. Solid line shows ridge axis.

13
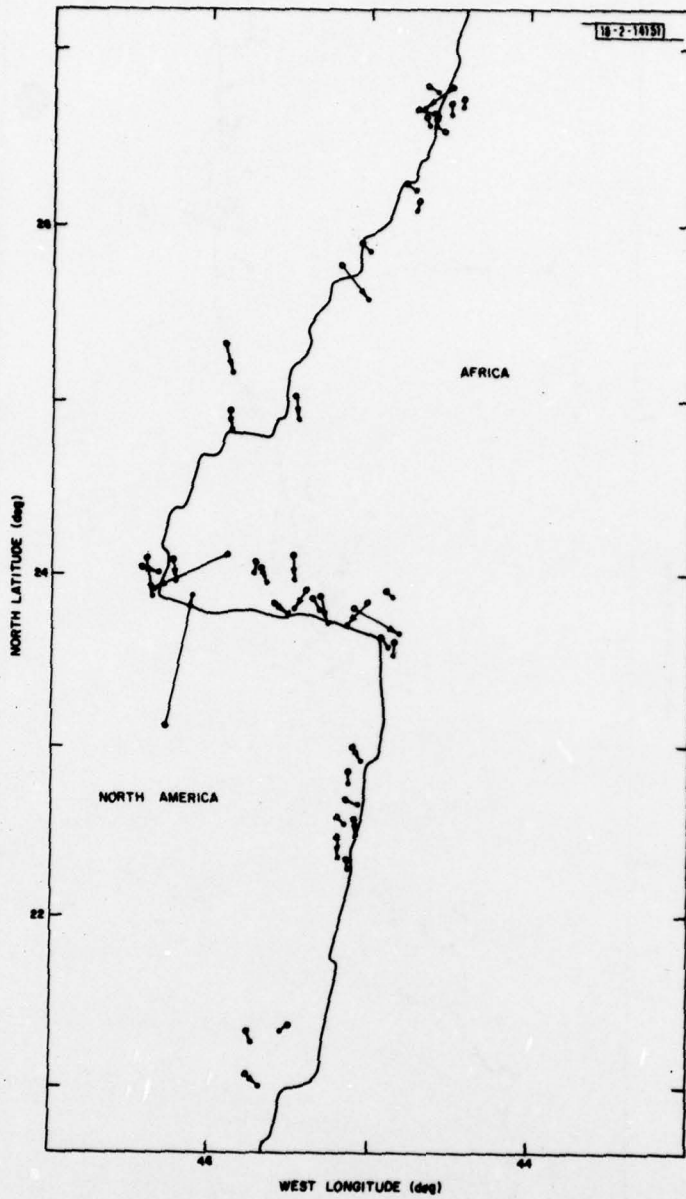
Fig. I-3. Chart showing relocation (solid circles) of ISC Bulletin epicenters (open circles) for North America and Africa using ocean ridge structure velocity model (ORM). Note closer grouping of epicenters about ridge axis for ORM relocated events. Events are for period 1964-1973. Solid line shows ridge axis.
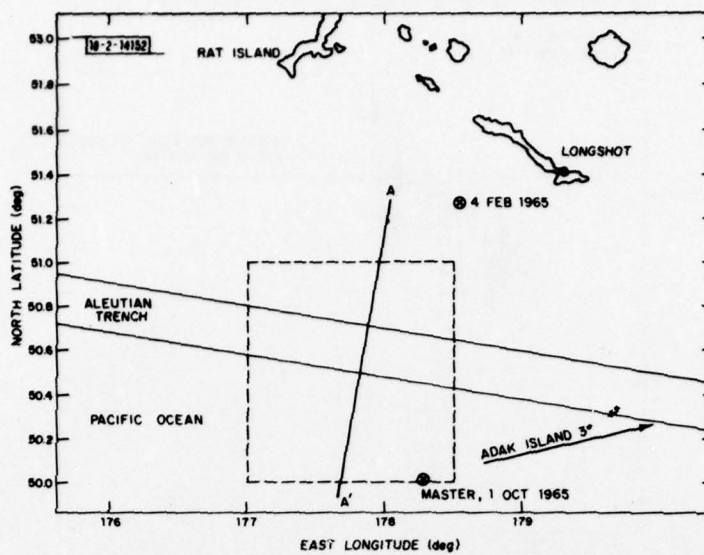
Fig. I-4. Rat Island source region: map view. Profile A-A' shown in Figs. I-6 and I-7.
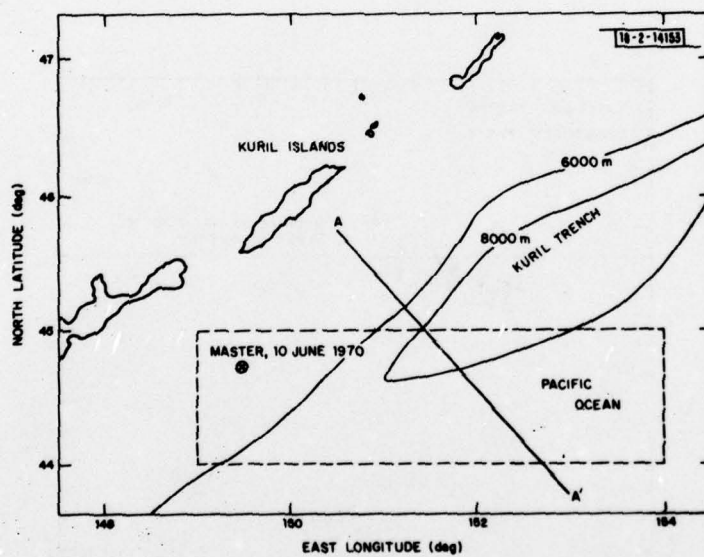
Fig. I-5. Kuril source region: map view. Profile A-A' shown in Fig. I-8.

15
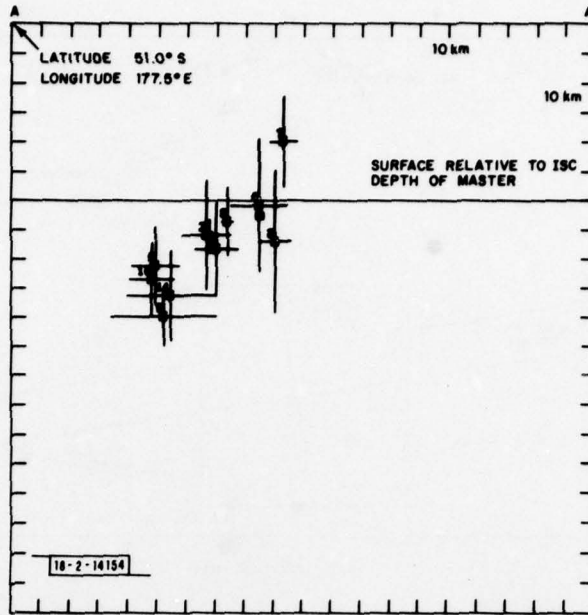
Fig. I-6. Rat Island relative location: 56° takeoff angle for ray path to ADAK.
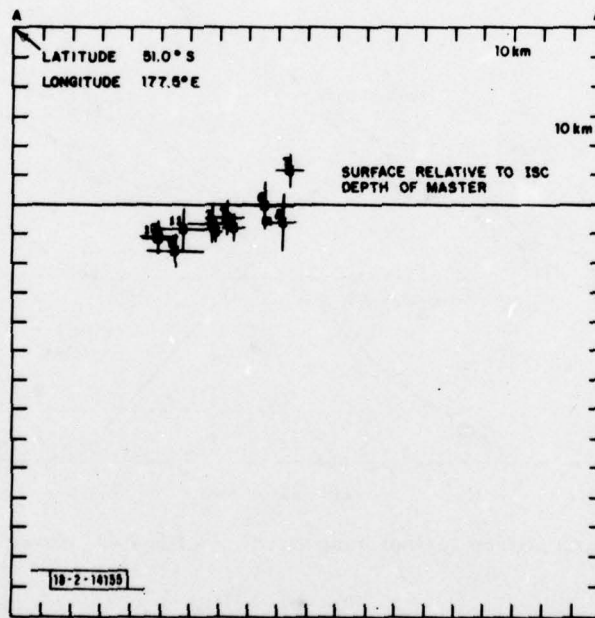
Fig. I-7. Rat Island relative locations: 95° takeoff angle for ray path to ADAK.
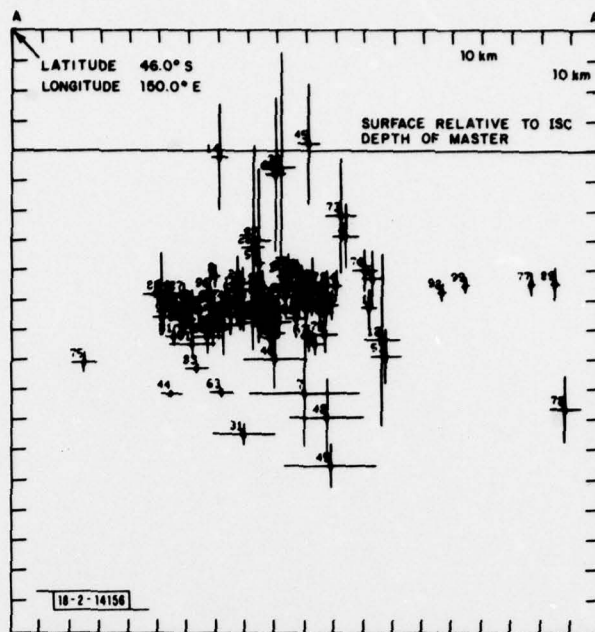
Fig. I-8. Kuril relative locations: uncertainties on one standard deviation.
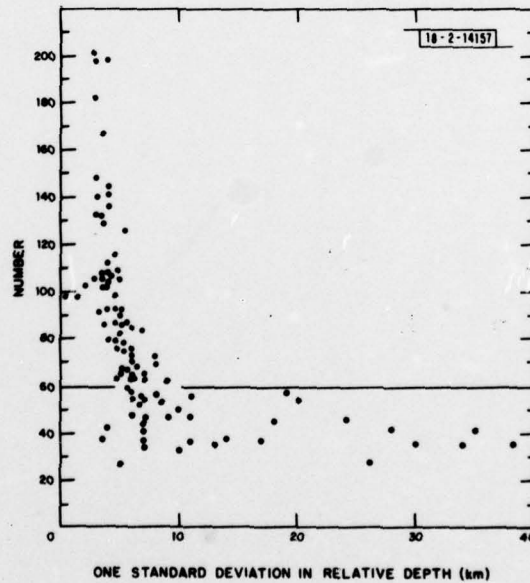
Fig. I-9. Size of Kuril data sets vs uncertainty in relative depth.

17

II. ESTIMATION OF SOURCE MOMENT TENSOR

A. INVERSION OF BODY-PHASE AMPLITUDES FOR THE MOMENT TENSOR

A mid-Atlantic earthquake that occurred on 23 October 1964 was chosen for this inversion experiment. The source region is beneath an abyssal plain and therefore free of major structural inhomogeneities. The body waves P, pP, and sP were well-recorded on the LP instruments of the WWSSN at a time when their seismometers had a 30-sec rather than the present 15-sec free period. The azimuthal coverage afforded by stations in Europe, North America, and Africa is as complete as can be expected from a teleseismic data set.

The analysis of the analog records proceeded as follows: LP vertical seismograms from 27 stations in the teleseismic distance range from 25° to 90° were digitized. DC and linear biases were removed, and linear interpolation was used to resample the data at a constant time increment of 0.25 sec. Examples of the resampled data are shown in Fig. II-1. To measure the relative excitations of p, pP, and sP the digitized seismograms were spiked by convolution with an inverse filter that removes the effect of the instrument and the anelasticity of the earth equivalent to a t* of 0.5. The effect of the inverse filter is illustrated in Figs. II-2 through II-4. The construction of filters of this kind is discussed in Robinson.[1] The raw filtered records contained high-frequency noise that is thought to be an unavoidable consequence of digitizing. To minimize this noise, various low-pass filters were applied to the spiked records. The most satisfactory one was a phaseless filter with a 12-dB-per-octave falloff at 1 Hz. Examples of these records are shown in Fig. II-5 with the phases identified.

The data for the moment tensor inversion were the amplitude of the appropriate spikes. The mean pP-P time of 10.5 sec and sP-P time of 14.7 sec are consistent with a source depth of about 45 km below the seafloor. In Fig. II-6 it is apparent that there is excellent coverage of one compressional quadrant of the focal sphere. The data set, 80 amplitudes, is sufficient to resolve significant differences from a standard double-couple source if such differences exist.

For moment tensor inversion, the amplitudes must be normalized for distance and free-surface effects. The distance effects include geometric spreading and anelasticity. The latter has been removed in an ad hoc manner by including a t* in the construction of the inverse filter. The former has been removed by first normalizing all amplitudes to an arc distance of 60° with an amplitude distance function derived from LP data presented in Sengupta and Julian.[2] A standard spreading factor for a distance of 60° was then used to reduce amplitude to the focal sphere.[3] The near-source conversion of s to P and p to P and the near-station effect of the free surface were removed by applying geometric ray theory to the case of plane waves incident on a free surface from a half space. The details of this part of this analysis follow Kanamori and Stewart.[4]

The reduced amplitudes were inverted for the moment tensor source representation using the formula derived by McCowan.[5] The solution revealed a source that contained 90-percent double couple, 9-percent compensated linear vector dipole, and 1-percent monopole — essentially a pure double couple as is assumed in first-motion solutions. The reduced amplitudes fit the model with an rms of 16 percent. However, in this case the nodal planes are oriented about 90° counterclockwise from planes inferred from a first-motion solution by Sykes and Sbar.[6] The contrasting double couples are summarized in Table II-1 and illustrated in Fig. II-6. The nodal amplitudes recorded at the three closest stations — BEC, SJG, and TRN — are, at a

19

TABLE II-1
DOUBLE COUPLE FROM MOMENT TENSOR INVERSION

	Strike		Slip		Dip
Nodal Plane 1	309		292		50
Nodal Plane 2	160		246		44

		Trend		Plunge	
Pole of Plane 2		70		45	
Pole of Plane 1		219		40	
P-axis		53		4	
T-axis		152		73	

Sykes and Sbar (Ref.6)

	Strike		Slip		Dip
Nodal Plane 1	44		315		57
Nodal Plane 2	286		221		53

		Trend		Plunge	
Pole of Plane 1		314		33	
Pole of Plane 2		195		37	
P-axis		164		3	
T-axis		258		54	

first glance, more consistent with the Sykes and Sbar solution; but the uncertainties in the takeoff angles to these stations, all in the distance range 9° to 15°, are sufficiently great that consistency with the inversion double couple can not be precluded. The P-axes (representing compressive stress) for both mechanisms are nearly horizontal; however, the orientation of the P-axis from the inversion double couple is more nearly normal to the mid-Atlantic ridge. Such an orientation is preferred by focal mechanisms of the thrust type in eastern North America and beneath the North Atlantic basin.[6] Inversion for the full moment tensor, as was done in this experiment, should yield source components that are less influenced by systematic errors in the reduced amplitudes than inversions for a constrained moment tensor as proposed by Strelitz.[7]

<div style="text-align:right">

T. J. Fitch
M. W. Shields
D. W. McCowan

</div>

B. STRUCTURAL INHOMOGENEITY AND THE RESOLUTION OF SOURCE FUNCTION

In a recent SATS,[5] Frasier and Fitch showed that long-period (LP) P-amplitudes from Cannikin varied as much from station-to-station as did the short-period (SP) amplitudes. The simplest, albeit indeterminate, explanation for this result is transmission of the seismic waves

through and around a structurally inhomogeneous source region for which there is ample geophysical evidence   Here, we investigate the effect of such amplitude distortion on inversions for the moment tensor source.

The Cannikin LP amplitudes in Fig. II-7, which are normalized to a distance of 60°, are consistent with a moment tensor source with 36-percent monopole, 57-percent double couple, and 7-percent compensated linear vector dipole (CLVD).   The double-couple component is superposed on the amplitude distribution in Fig. II-7.   The degree of amplitude distortion from near-source structure is probably near an upper limit for this case.   The frequency content of these signals is concentrated near the high-frequency end of the teleseismic source spectrum in the bandpass 1 to 0.2 Hz, and the structural inhomogeneity associated with the Aleutian arc and subduction may involve velocity contrasts of about 5 to 10 percent over horizontal distances of tens to hundreds of kilometers.

To add credibility to the interpretation of the Cannikin amplitudes, a similar analysis was carried out with P-wave amplitudes from an intermediate earthquake located about 5° east of the test site on Amchitka.   Figure II-8 shows that, as in the case of the Cannikin amplitudes, those for the earthquake show nearly as much LP or SP variation.   In this case, the LP amplitudes are dominated by spectral components near the 15-sec peak in instrument response.   The apparent moment tensor representation is 60-percent double couple, 29-percent CLVD, and 11-percent monopole.   A large compressional amplitude at College Station (COL in Fig. II-9) accounts for about one-third of the CLVD component.   Instrument polarity at this station has been found to be correct.   The non-double-couple components are likely to be artifacts of an incomplete data set and amplitude distortion.   Figure II-9 shows the distribution of first-motion and the double-couple component.

If the same analysis is applied to LP P-amplitudes from sources in structurally less-complex parts of the world, the double couple (in the case of earthquakes) and the monopole (in the case of explosions) dominates the moment tensor representations.   For example, the Borrego Mountain earthquake in Southern California yielded 81-percent double couple, 13-percent CLVD, and 6-percent monopole.   The plot of LP vs SP amplitudes in Fig. II-10 shows a distinct elongation along the SP axis which is expected in cases where large-scale structural complexity is absent in the same region.   The amplitude distribution and double-couple component are shown by McCowan elsewhere in this SATS.   A Novaya Zemlya explosion[5] has a much-more-uniform amplitude distribution than Cannikin (Fig. II-11).   The moment tensor components are 62-percent monopole, 34-percent double couple, and 3-percent CLVD.

In this study, loose upper bounds have been placed on the effect of amplitude distortion on moment tensor sources.   Structurally related distortion can not be removed by any known scheme.   Consequently, such distortion remains a major obstacle to the resolution of source functions, particularly where sources are located in structurally complex regions.

<div align="right">

T. J. Fitch
M. W. Shields

</div>

C.   ESTIMATING FAULT-PLANE SOLUTIONS BY ROBUST METHODS

Finding fault-plane solutions for earthquakes (or explosions) remains one of the last examples of manual drudgery in seismological research.   Unfortunately, the procedure is a familiar one.   First the data, usually LP polarities, are read either from film or digital

recordings. Next, each data point is plotted on a stereographic projection of the lower focal hemisphere. Then, the fault-plane solution is found by manipulating a stereonet on top of the data projection. Usually, there is a spectrum of allowable fault-plane solutions which will satisfy the data so, finally, bounds on the solution are estimated by mapping out extreme values with the stereonet.

The objective of this research is twofold: first, to reduce the considerable labor involved; and second, to remove (as much as possible) the subjective element. Both these difficulties are common sources of error. It is hoped that removing them will improve routine fault-plane solutions and therefore lead to better discrimination between earthquakes and explosions.

The operational problems involved in finding fault-plane solutions are threefold. First, the data consist only of inequalities which will, of course, admit a wide variety of models. Second, the data must be corrected by projecting them back through the transmitting earth to the focal sphere, which, of necessity, implies the assumption of an earth model. Third, the data are satisfied by an ad hoc trial-and-error procedure of fitting the model, which involves an element of subjective judgment.

The first problem in the procedure can be solved easily by using the LP P-wave amplitudes themselves instead of just their signs. There is, it turns out, very little extra labor involved in measuring and recording the relative amplitudes on paper as there is in noting their signs. Unfortunately, the second problem then becomes significant. Finding where a ray took off from the focal sphere to a given station is far easier than correcting its amplitude observed on the surface of the earth back to the source. On the other hand, if properly corrected amplitudes are available, then the third problem is virtually solved because deterministic estimation schemes can be readily employed.

So, the major stumbling block would appear to be in correcting the amplitude observations back to the source. In fact, there is another small problem which places a constraint on any practical method. Frequently, due to variations in signal-to-noise ratio (S/N), it is not possible to measure an amplitude accurately but it is still possible to observe its polarity. Any workable method must therefore allow data that can be either amplitudes or just signs.

We attempted to solve the second problem by adopting an estimation procedure based on minimizing the L1 norm. The method, as formulated by Claerbout and Muir,[8] is a way of finding the optimum linear model which minimizes the sum of the absolute differences between itself and the data. This is opposed to the usual least-squares, or L2, norm which minimizes the sum of the squares of the corresponding differences. The L1 norm has two important advantages over the L2 norm: first, it is less sensitive to erroneous data values, a property called robustness; and second, it conveniently allows data that consist only of inequalities. We applied the method by fitting the linear point source moment tensor model[5] directly to the film-chip amplitudes and polarities. In this way, correcting those amplitudes back to the source was completely neglected. Because of its robust properties, the L1 norm estimates linear models which are less sensitive to such a gross omission as would be those estimated by minimizing an L2 norm.

To illustrate the method, we chose two events: the Borrego Mountain earthquake of 9 April 1968, and a deep Fiji-Tonga earthquake of 9 October 1967. An analyst read the LP amplitudes for both events from WWSSN film chips. Figures II-12 and II-13 show equal-area projections of the lower focal hemisphere of the Borrego Mountain earthquake with the data and fault planes indicated for the L1 and L2 norms, respectively. In the latter case (as in the other L2 norm

22

examples given below), the solution was constrained to have no volume change. Both solutions are similar in that they show a predominance of double-couple source mechanism with a strike slip orientation. Figures II-14 and II-15 show the same cases except that the amplitude of one data point has been multiplied by ten. As can be seen, the L1 solution is still much the same as it was, but the L2 solution is completely different — it is still dominated by a strike slip double couple but has been rotated by nearly 45°. This example illustrates the robust property of the L1 estimate.

Figures II-16 through II-18 show results for the Fiji-Tonga earthquake. Figure II-16 is an L1 norm estimate using all the LP amplitude and polarity data, and Fig. II-17 is an L2 norm solution using just the LP amplitudes. Both are similar, although the L2 norm solution has significantly more double-couple mechanism in it. Figure II-18 is the same as Fig. II-16, but with an additional nine near-in SP polarities added. Clearly, this solution is much better in terms of resolution than the other two; it is composed of principally double-couple source mechanism. So, the inclusion of a few additional polarities completely changes a fault-plane solution both in terms of its orientation and force composition. If we were to restrict ourselves to using just amplitude data, the inclusion of these critical data points would not have been possible.

These results suggest that a balanced approach to calculating fault-plane solutions based on minimizing the L1 norm of LP amplitude residuals supplemented by reliable first-motion (polarity) data may be practical in general usage. It is a convenient way of blending in the first-motion data, and is relatively insensitive to erroneous data values.

<div align="right">D. W. McCowan</div>

D. SYNTHETIC SEISMOGRAMS BY SUPERPOSITION OF NORMAL MODES: APPLICATION TO THE INVERSE PROBLEM FOR SOURCE MECHANISM

Current expansion of the world-wide network of stations with digital recording should make possible routine determination of the moment tensor of seismic sources. The effects of lateral heterogeneities may impose certain restrictions on the upper limit of the frequency range. Also, it may be necessary to avoid, at first, surface waves whose dispersion is a strong function of the structure in the most heterogeneous part of the earth.

The purpose here is to describe an algorithm that can be used to efficiently generate synthetic seismograms by superposition of normal modes, and to show application of the method to the direct and inverse problem of importance in seismology. Although only the modes that were obtained by the exact solution will be used here, the method can be easily combined with results of computations at higher frequencies by approximate methods that are faster and sufficiently accurate.

Following Gilbert and Dziewonski,[9] the displacement function in epicentral coordinates can be written as

$$u(r, t) = \sum_{i=1}^{6} M_i(t) * \sum_{n=0}^{\infty} \sum_{\ell=0}^{\infty} {}_n f_\ell(t) \sum_m {}_n s_\ell^m(r) \cdot [{}_n \bar{\epsilon}_\ell^m(r_o)]_1 \quad .$$

where $M_i(t)$ are the six independent components of the moment tensor as a function of time and

$${}_n f_\ell(t) = \{1 - \cos {}_n \omega_\ell t \cdot \exp[- {}_n \omega_\ell t / 2 {}_n Q_\ell]\} \cdot H(t)$$

describes the temporal behavior of each individual mode. Summation over m extends from $-\min(2,\ell)$ to $\min(2,\ell)$. Our notation follows that in Ref. 9, and will not be fully explained here. We note that the effect of the geographical coordinates of the receiver is the same for all the modes of the same angular order ℓ. Thus, for a given mode type and angular order number, contribution of all the overtones can be evaluated first — the corresponding functions will depend on the source radius r_o, receiver radius (usually equal to the radius of the earth — a), and time. For spheroidal modes, one needs to evaluate four functions for vertical as well as horizontal displacements:

$$\begin{matrix} U_{1\ell} \\ V_{1\ell} \end{matrix} = \sum_n \begin{matrix} {}_nU_\ell(a) \\ {}_nV_\ell(a) \end{matrix} \cdot {}_n\dot{V}_\ell(r_o) \cdot {}_nf_\ell(t)$$

$$\begin{matrix} U_{2\ell} \\ V_{2\ell} \end{matrix} = r_o^{-1} \sum_n \begin{matrix} {}_nU_\ell(a) \\ {}_nV_\ell(a) \end{matrix} \cdot [{}_nU_\ell(r_o) - \tfrac{1}{2}\ell(\ell+1)\,{}_nV_\ell(r_o)]\,{}_nf_\ell(t)$$

$$\begin{matrix} U_{3\ell} \\ V_{3\ell} \end{matrix} = \sum_n \begin{matrix} {}_nU_\ell(a) \\ {}_nV_\ell(a) \end{matrix} \{{}_n\dot{V}_\ell(r_o) + [{}_nU_\ell(r_o) - {}_nV_\ell(r_o)]/r_o\}\,{}_nf_\ell(t)$$

$$\begin{matrix} U_{4\ell} \\ V_{4\ell} \end{matrix} = r_o^{-1} \sum_n \begin{matrix} {}_nU_\ell(a) \\ {}_nV_\ell(a) \end{matrix} {}_nV_\ell(r_o)\,{}_nf_\ell(t) \quad .$$

For toroidal modes there are only two functions, denoted $W_{3\ell}$ and $W_{4\ell}$ because of their analogy with $V_{3\ell}$ and $V_{4\ell}$:

$$W_{3\ell} = \sum_n {}_nW_\ell(a)\,[{}_n\dot{W}_\ell(r_o) - {}_nW_\ell(r_o)/r]\,{}_nf_\ell(t)$$

$$W_{4\ell} = r_o^{-1} \sum_n {}_nW_\ell(a)\,{}_nW_\ell(r_o)\,{}_nf_\ell(t) \quad .$$

Examples of functions $U_{i\ell}$, $V_{i\ell}$, and $W_{i\ell}$ computed for a source depth of 650 km and $\ell = 4$ are shown in Fig. II-19. The appropriate eigenfunctions and eigenfrequencies were computed by Buland[10] for the earth model 1066B (Ref. 9); the quality factors ${}_nQ_1$ were obtained using the anelastic structure of the model FSQMK of Dziewonski.[5,11] The time traces represent superposition of the modes with periods from 1545 sec ($_0S_4$) to 45 sec ($_{60}S_4$). Because of the low angular order number, at high frequencies the compressional waves can be associated with PKIKP close to 180° and shear waves with nearly vertical ScS reflections. The sharp onset on U_1 is the arrival of a P-wave to the surface from the depth of 650 km; the corresponding feature for S can be seen on V_3 or W_3. The pairs of SP pulses on the trace U_1 correspond to PKIKP and pPKIKP; their multiple reflections are gradually attenuated due to finite Q and internal reflections from discontinuities. ScS and sScS can be easily seen on V_3 and W_3; the SP behavior of these two functions is very similar, as could be expected for S_V and S_H at nearly vertical incidence.

Once the library of functions U, V, and W has been prepared, they can be used to compute rapidly synthetic seismograms for an arbitrary source mechanism and location of the receiver.

The complete expressions are rather tedious and will be omitted here; they are analogous to Eqs. (2.1.30) and (2.1.31) of Gilbert and Dziewonski,[9] and represent products and sums of functions $U_{j\ell}$, $V_{j\ell}$, and $W_{j\ell}$ with the appropriate spherical harmonics of degree 1 and their derivatives:

$$u_i(a,\Theta,\phi,t) = \sum_{k=1}^{6} M_k(t) * \sum_{\ell=0}^{\ell_{max}} A_{ik\ell} [(r_o,a,t),(\Theta,\phi)] \quad .$$

Finally, after summation over ℓ:

$$u_i(r,t) = \sum_{k=1}^{6} M_k(t) * B_{ik}(r,t) \quad .$$

The functions $B_{ik}(r,t)$ represent, in effect, the Green's functions for each of the six independent elements of the moment rate tensor associated with a point source.

Figures II-20 through II-22 are record sections from 10° to 180° computed for the vertical, longitudinal, and transverse components of an instrument with a WWSSN response. The source mechanism used was the fault-plane solution of Mendiguren[12] for the Colombian earthquake of 31 July 1970. A number of commonly observed body-wave phases are identified in the figures; the effect of antipodal focusing at 180° is quite spectacular. Computation of 54 seismograms shown, each containing contributions of nearly 6000 normal modes, required only 15 min. on a minicomputer.

If the source mechanism can be represented by a point source in time, then the convolution operation in the equation above is replaced by multiplication, and the inverse problem is linear in the time domain (it is always linear in the frequency domain). Examples of application of this approach have been demonstrated by Stump and Johnson[13] for sources imbedded in an elastic half-space. The following experiment is designed to show the stability of the inverse solution in the presence of noise for a realistic, spherically symmetric earth model with anelastic attenuation.

Mendiguren's mechanism of the Colombian earthquake [in equivalent moment tensor representation; cf. Gilbert and Dziewonski,[9] Eq. (3.2.1)] was used to compute three 3-component synthetic spectra at an epicentral distance of 90° and azimuths of 0°, 120°, and 240°. The inverse problem for the moment tensor was then solved for various levels of random noise added to the synthetic spectra.

Table II-2 lists the results of inversion, with standard errors of the elements of the moment tensor, for different noise levels. A noise level of 100 percent means that the rms spectral amplitude of the noise is equal to the rms amplitude of the signal, within the frequency band of interest. The solution is very close to the exact values, even with 200-percent noise. The statistically estimated standard errors are in good agreement with the level of differences between computed and exact values. This also applies to the isotropic component of the moment tensor, whose value should be zero for the double couple, of course.

An explanation of the stability of the solution is that we have used seismograms that contain body waves leaving the focus at great many angles of incidence. Thus, even though we used only records from three different sites, the sampling of the focal sphere was quite thorough. Also,

TABLE II-2

INVERSION FOR ELEMENTS OF THE MOMENT TENSOR

(Three 3-Component WWSSN Stations at 90°, Azimuth = 0°, 120°, and 240°)

	M_{rr}	$M_{\theta\theta}$	$M_{\varphi\varphi}$	$M_{r\theta}$	$M_{r\varphi}$	$M_{\theta\varphi}$	1/3 Trace (Moment Tensor)
Input	−0.890	0.135	0.754	−0.301	0.314	−0.346	0
+50-Percent Noise	−0.891 ± 0.003	0.136 ± 0.003	0.757 ± 0.003	−0.301 ± 0.001	0.316 ± 0.001	−0.347 ± 0.001	0.001 ± 0.003
+100-Percent Noise	−0.901 ± 0.006	0.122 ± 0.007	0.737 ± 0.007	−0.303 ± 0.002	0.314 ± 0.002	−0.346 ± 0.002	−0.014 ± 0.006
+200-Percent Noise	−0.882 ± 0.012	0.148 ± 0.013	0.763 ± 0.013	0.299 ± 0.005	0.312 ± 0.005	−0.350 ± 0.004	0.010 ± 0.012

it appears that one could obtain a reliable solution with less information than has been used in this particular example. This would allow for exclusion from the analysis portions of the seismograms that are severely contaminated by the effect of lateral heterogeneities — the fundamental mode surface waves, for example. Then, with the source mechanism known, the phase and group velocities could be measured for the particular path. Such an iterative procedure might represent a valuable tool in the studies on the characteristics of surface-wave propagation.

A. M. Dziewonski

E. A MOMENT TENSOR FORMULATION OF ALEKSEYEV'S AND MIKHAYLENKO'S ELASTIC-WAVE METHOD

To solve vertically inhomogeneous elastic-wave problems, A. S. Alekseyev and B. G. Mikhaylenko[14] have proposed a different method which combines separation of variables with finite differences. They employ the Hankel transform to remove the radial dependence of the solution as in the reflectivity method, but solve the remaining problem in time and depth by finite differences. The complete solution must then be reconstructed by numerically integrating the inverse Hankel transform. In a further development (unpublished), they have removed that final numerical integration by a Hankel series technique. Although it is still too early to assess their method in regards to its competitors (finite difference, finite element, reflectivity, and Cagnaird-de Hoop), it is worth noting that it allows only simple source models. Here we attempt to reformulate Alekseyev's and Mikhaylenko's equations in a moment tensor form which will allow any point source mechanism.

The equations of motion in cylindrical coordinates can be written as a Hankel transform[15]:

$$\vec{s}(r,\phi,z,t) = \sum_{m=-\infty}^{+\infty} \int_0^\infty k\,dk\,[r_1(k,z,t,m)\,\vec{R}_m^1(kr,\phi) + r_2(k,z,t,m)\,\vec{R}_m^2(kr,\phi)$$

$$+ \ell(k,z,t,m)\,\vec{L}_m(kr,\phi)]$$

which, in vector notation, reads:

$$\vec{s}(r,\phi,z,t) = \sum_{m=-\infty}^{+\infty} \int_0^\infty k\,dk\,C_m(kr,\phi)\,\vec{G}_m(k,z,t)$$

where the C matrix and $\vec{C}$ vector are

$$C_m(kr,\phi) \equiv \begin{bmatrix} 0 & J'_m & \frac{im}{kr}\,J_m \\ 0 & \frac{im}{kr}\,J_m & -J'_m \\ J_m & 0 & 0 \end{bmatrix} \qquad \vec{G}_m(k,z,t) \equiv \begin{bmatrix} r_1(k,z,t,m) \\ r_2(k,z,t,m) \\ \ell(k,z,t,m) \end{bmatrix} \quad .$$

The closure-completeness relation is

$$\int_0^{2\pi} d\phi \int_0^\infty r\,dr\,C_m^+(k'r,\phi)\,C_n(kr,\phi) = \frac{2\pi\delta(k-k')}{\sqrt{kk'}}\,\delta_n^m\,I \quad .$$

27

If this form of the solution is substituted into the elastic equation of motion where the elastic properties depend only on depth, the equations reduce to the Alekseyev and Mikhaylenko form. Strictly speaking, however, the right-hand-side force density vector must be similarly transformed for a complete simplification to occur.

In the, now common, moment tensor representation,[16] the force density vector is written:

$$\vec{F} = -\nabla \cdot [M\delta(\vec{r} - \vec{r}_s)] = \sum_{m=-2}^{+2} \int_o^\infty kdk\, C_m(kr,\phi)\, \vec{H}_m(k,z,t)$$

where

$$\vec{H}_m(k,z,t) \equiv \begin{bmatrix} d(k,z,t,m) \\ e(k,z,t,m) \\ f(k,z,t,m) \end{bmatrix} \implies \vec{H}_m(k,z,t) = -\frac{1}{2\pi} \int_o^{2\pi} d\phi \int_o^\infty rdr$$

$$\times\, C_m^+(kr,\phi)\, \nabla \cdot [M\delta(\vec{r} - \vec{r}_s)] \quad .$$

If the moment tensor is expressed in north, east, and down components as before, then explicit expressions for the $\vec{H}$ vector are obtained:

$$d(k,z,t,m) = -\frac{M_{ZZ}}{2\pi}\delta_0^m + \frac{\delta(z-z_s)}{2\pi}\left(\frac{k}{2}\right)[M_{NZ}(\delta_1^m - \delta_{-1}^m) - iM_{EZ}(\delta_1^m + \delta_{-1}^m)]$$

$$e(k,z,t,m) = -\frac{(M_{NN} + M_{EE})}{2\pi}\left(\frac{k}{2}\right)\delta(z-z_s)\delta_0^m + \frac{(M_{NN} - M_{EE})}{2\pi}\left(\frac{k}{4}\right)(\delta_2^m + \delta_{-2}^m)$$

$$\times\, \delta(z-z_s) - \frac{M_{NE}}{2\pi}\left(\frac{ik}{2}\right)(\delta_2^m - \delta_{-2}^m)\delta(z-z_s) - \frac{1}{2\pi}\frac{\delta'(z-z_s)}{2}$$

$$\times\, [M_{NZ}(\delta_1^m - \delta_{-1}^m) - iM_{EZ}(\delta_1^m + \delta_{-1}^m)]$$

$$f(k,z,t,m) = -\frac{(M_{NN} - M_{EE})}{2\pi}\left(\frac{ik}{4}\right)(\delta_2^m - \delta_{-2}^m)\delta(z-z_s) - \frac{M_{NE}}{2\pi}\left(\frac{k}{2}\right)(\delta_2^m + \delta_{-2}^m)$$

$$\times\, \delta(z-z_s) + \frac{1}{2\pi}\frac{\delta'(z-z_s)}{2}[iM_{NZ}(\delta_1^m + \delta_{-1}^m) + M_{EZ}(\delta_1^m - \delta_{-1}^m)] \quad .$$

Putting everything together gives the desired result:

$$\left\{ \begin{bmatrix} \lambda + 2\mu & 0 & 0 \\ 0 & \mu & 0 \\ 0 & 0 & \mu \end{bmatrix} \frac{\partial^2}{\partial z^2} + \begin{bmatrix} \lambda' + 2\mu' & -k(\lambda + \mu) & 0 \\ k(\lambda + \mu) & \mu' & 0 \\ 0 & 0 & \mu' \end{bmatrix} \frac{\partial}{\partial z} + \begin{bmatrix} -k^2\mu & -k\lambda' & 0 \\ k\mu' & -k^2(\lambda + 2\mu) & 0 \\ 0 & 0 & -k^2\mu \end{bmatrix} \right.$$

$$\left. - \begin{bmatrix} \rho & 0 & 0 \\ 0 & \rho & 0 \\ 0 & 0 & \rho \end{bmatrix} \frac{\partial^2}{\partial t^2} \right\} \vec{G}_m(k,z,t) = - \begin{bmatrix} \rho & 0 & 0 \\ 0 & \rho & 0 \\ 0 & 0 & \rho \end{bmatrix} \vec{H}_m(k,z,t)$$

which is a moment tensor form of Alekseyev's and Mikhaylenko's result.

D. W. McCowan

REFERENCES

1. E. A. Robinson, <u>Multichannel Time Series Analysis With Digital Computer Programs</u> (Holden-Day, San Francisco, 1967), p. 298.

2. M. K. Sengupta and B. R. Julian, "P-Wave Travel Times from Deep Earthquakes," Bull. Seismol. Soc. Am. 66, 1555-1579 (1976), DDC AD-A042240/2.

3. R. L. Wesson, "A Time Integration Method for Computation of the Intensities of Seismic Rays," Bull. Seismol. Soc. Am. 60, 307-316 (1970).

4. H. Kanamori and G. S. Stewart, "Mode of the Strain Release Along the Gibbs Fracture Zone, Mid-Atlantic Ridge," Phys. Earth Planet. Inter. 11, 312-332 (1976).

5. Seismic Discrimination SATS, Lincoln Laboratory, M.I.T. (31 March 1977), DDC AD-A045453/8.

6. L. R. Sykes and M. L. Sbar, "Intraplate Earthquakes, Lithospheric Stress and the Driving Mechanism of Plate Tectonics," Nature 245, 298-302 (1973).

7. R. A. Strelitz, "Moment Tensor Inversion and Source Models," Geophys. J. R. Astr. Soc. 52, 359-364 (1978).

8. J. F. Claerbout and F. Muir, "Robust Modeling With Erratic Data," Geophysics 38, 826-844 (1973).

9. F. Gilbert and A. M. Dziewonski, "An Application of Normal Mode Theory to the Retrieval of Structural Parameters and Source Mechanisms from Seismic Spectra," Philos. Trans. R. Soc. London 278, 187-269 (1975).

10. R. P. Buland, "Retrieving the Seismic Moment Tensor," Ph. D. Thesis. University of California, San Diego (1976).

11. A. M. Dziewonski, "Finite Strain Model of the Earth With Consideration of Velocity Dispersion," Trans. Am. Geophys. Union 58, 439 (1977), abstract.

12. J. Mendiguren, "Identification of Free Oscillation Spectral Peaks; 1970 July 31, Colombian Deep Shock Using the Excitation Criterion," Geophys. J. R. Astr. Soc. 33, 281-321 (1973).

13. B. W. Stump and L. R. Johnson, "The Determination of Source Properties by the Linear Inversion of Seismograms," Bull. Seismol. Soc. Am. 67, 1489-1502 (1977).

14. A. S. Alekseyev and B. G. Mikhaylenko, "Solution of Lamb's Problem for a Vertically Inhomogeneous Halfspace," Izv. Earth Phys. 12, 11-25 (1976).

15. D. W. McCowan, "Moment Tensor Representation of Surface Wave Sources," Geophys. J. R. Astr. Soc. 44, 595-599 (1976), DDC AD-A037625/1.

16. F. Gilbert, "Excitation of the Normal Modes of the Earth by Earthquake Sources," Geophys. J. R. Astr. Soc. 22, 223-226 (1970).
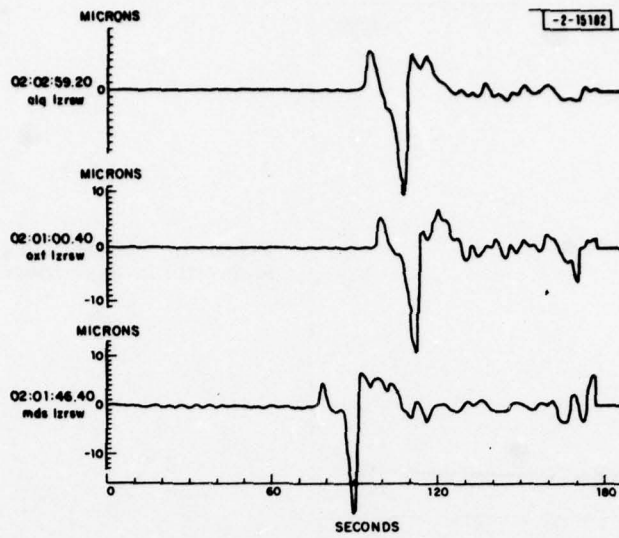
Fig. II-1. Sample of digitized wave forms.
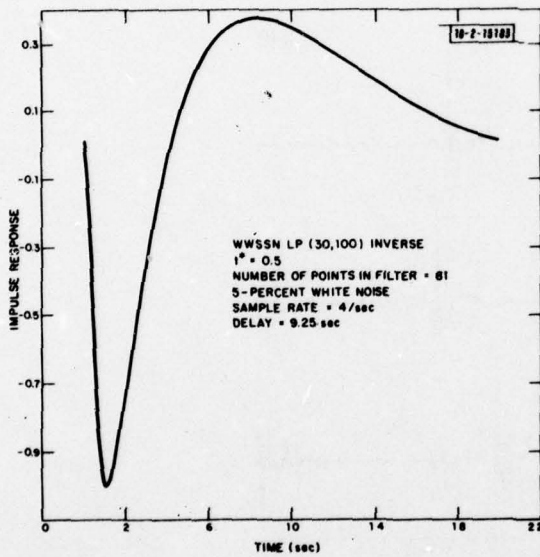
Fig. II-2. Synthetic wave form used
in construction of inverse filter.
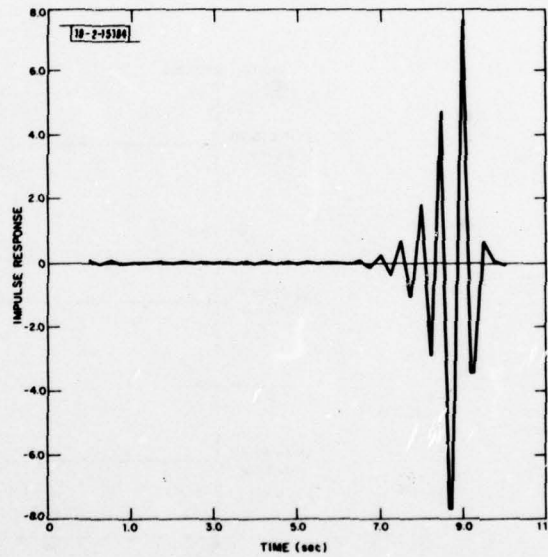
Fig. II-3. Inverse filter in time domain.

31
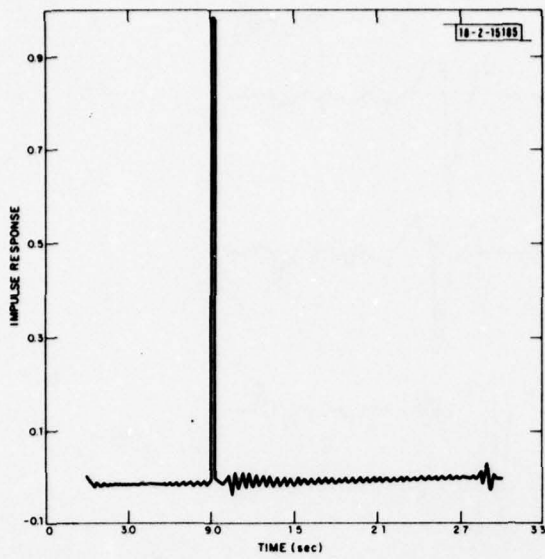
Fig. II-4. Convolution of synthetic wave form with inverse filter.
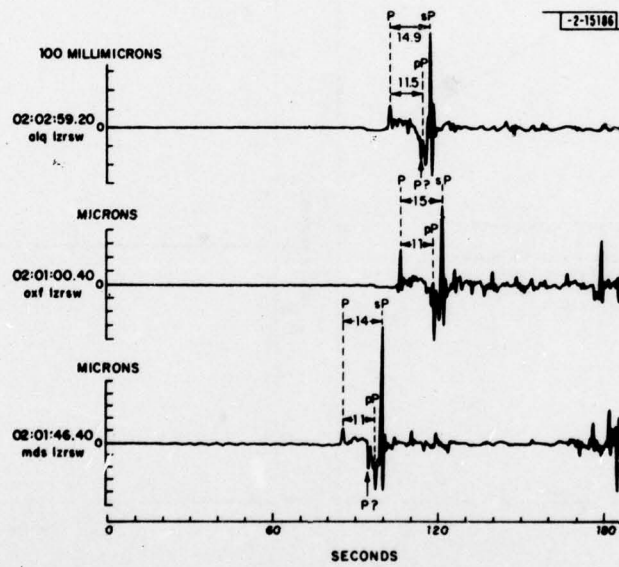
Fig. II-5. Sample convolution of real wave forms with inverse filter.
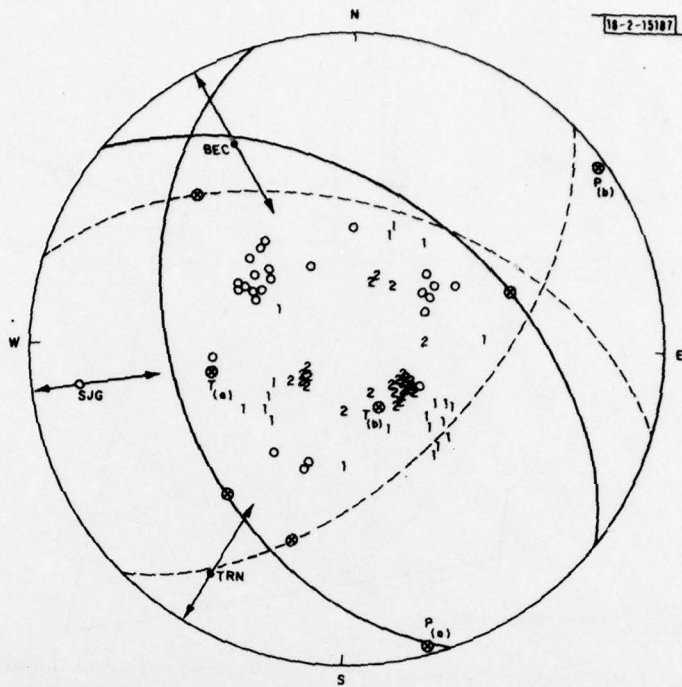
32

Fig. II-6. Double couples superimposed on focal sphere: equal area project of lower hemisphere.

COMPRESSIONAL QUADRANT
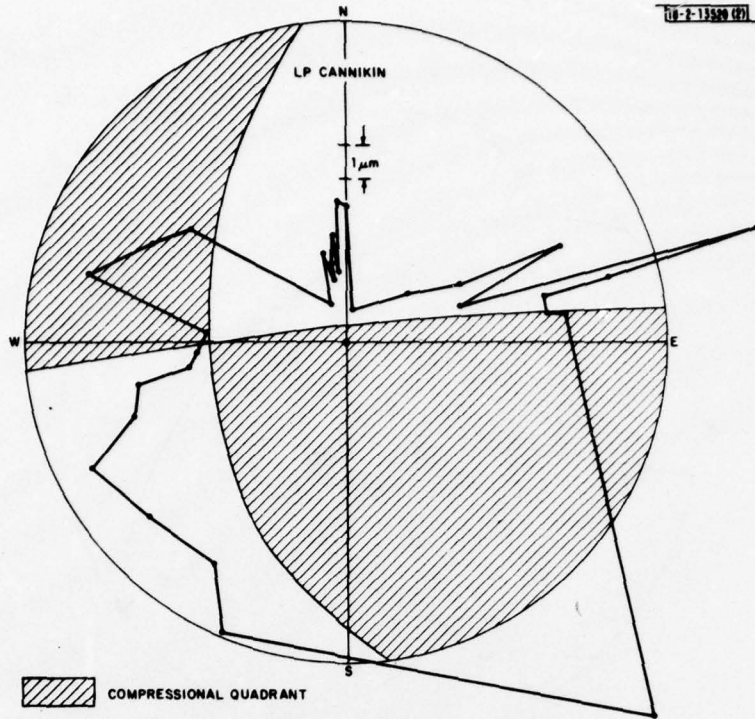
Fig. II-7. LP P-wave amplitude from Cannikin and apparent double-couple component: only azimuthal amplitude variation is illustrated, whereas double-couple component is projected in equal-area sense on lower half of focal sphere.
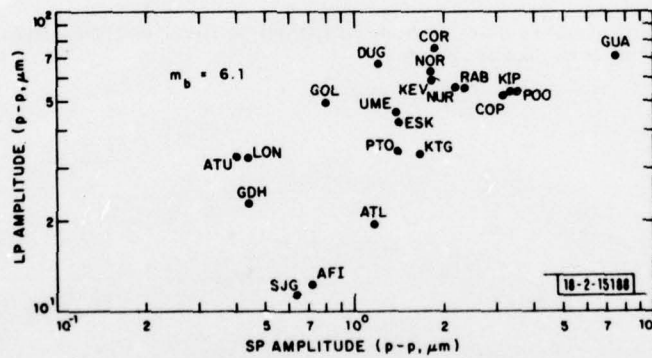
Fig. II-8. LP vs SP amplitude variation for Aleutian intermediate-depth earthquake, 28 February 1970.
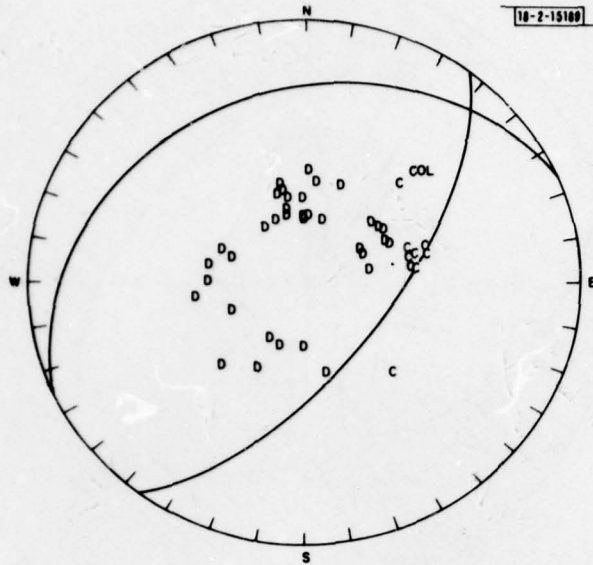
Fig. II-9.   First-motion polarities of Aleutian earthquake and apparent double-couple source component.
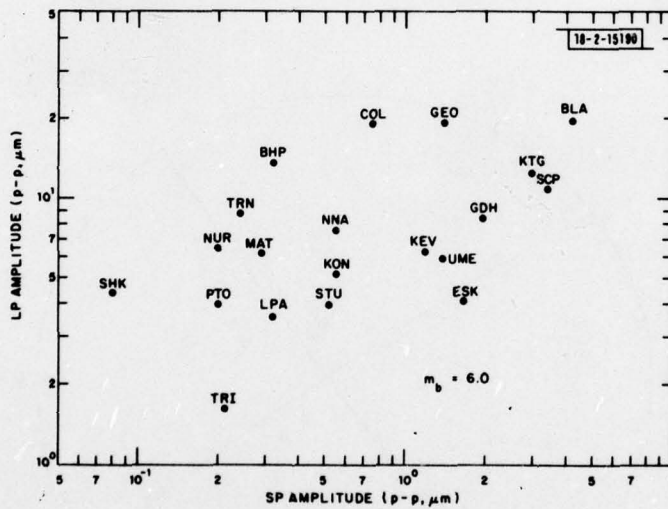
Fig. II-10.   LP vs SP amplitude variation for Borrego Mountain, California earthquake, 9 April 1968.
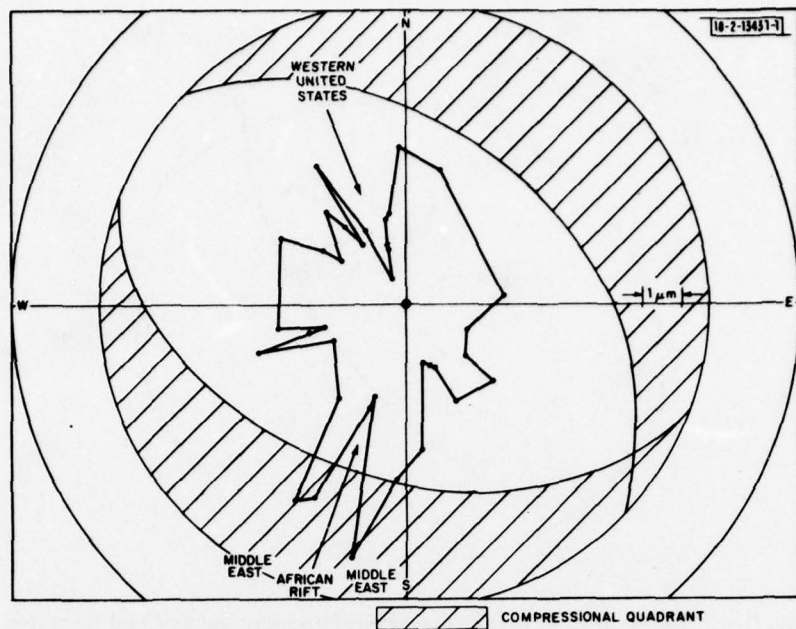
Fig. II-11.   LP P-wave amplitude from Novaya Zemlya explosion,
14 October 1970, and apparent double-couple component.
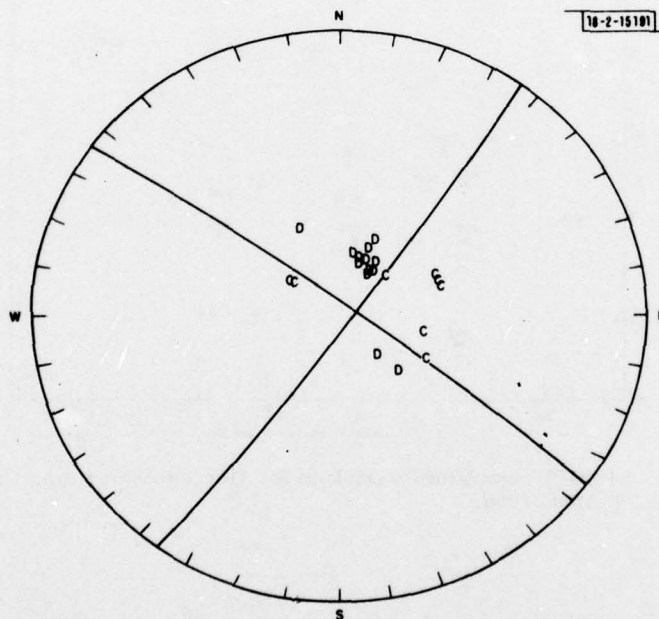
Fig. II-12.   Fault-plane solution for Borrego Mountain earthquake.   Equal-area
projection of lower focal hemisphere with C = compression and D = dilation.
L1 norm estimate with 2.7-percent monopole, 8.3-percent dipole, and 89.0-percent
double couple.
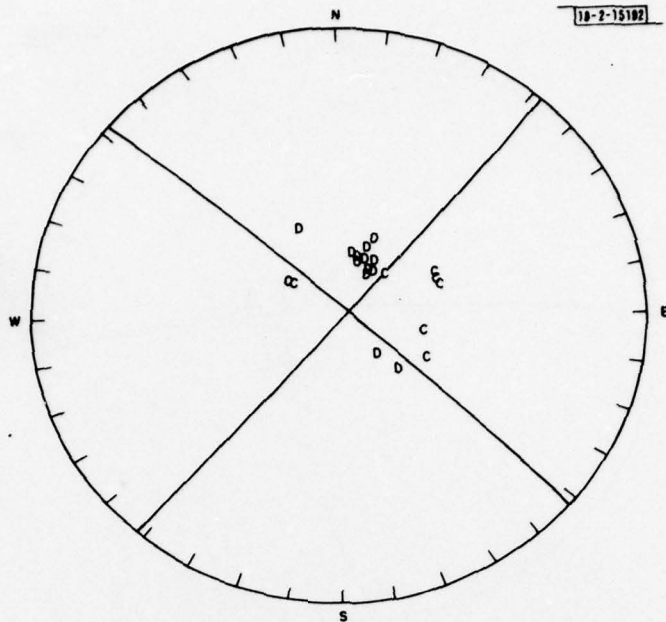
Fig. II-13. Fault-plane solution for Borrego Mountain earthquake. L2 norm estimate with 0.8-percent dipole and 99.2-percent double couple.
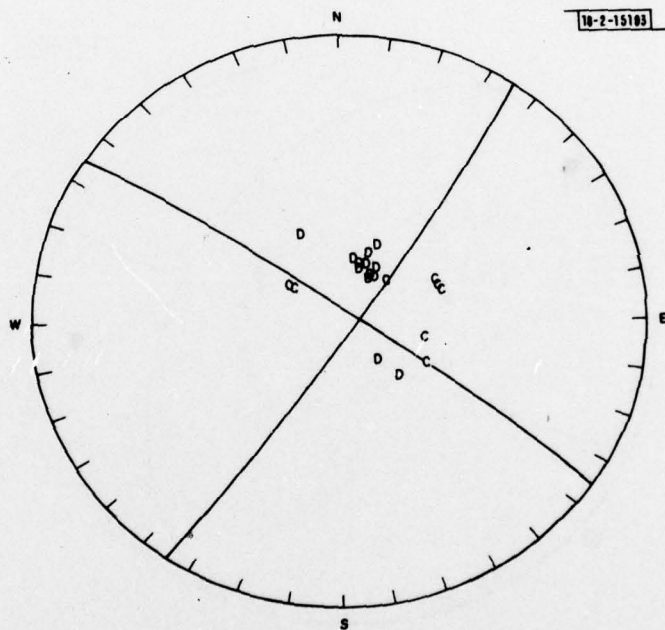
Fig. II-14. Fault-plane solution for Borrego Mountain earthquake. L1 norm estimate with 6.1-percent monopole, 16.5-percent dipole, and 77.3-percent double couple. One data point has been artificially amplified by a factor-of-10.
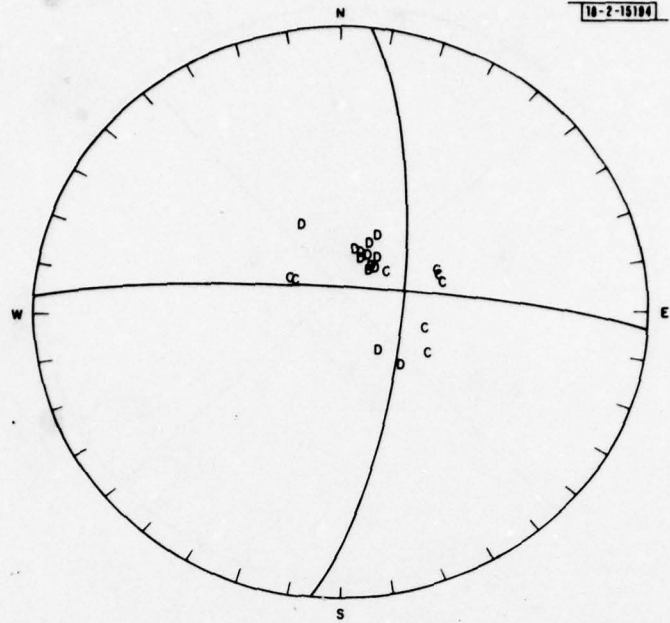
Fig. II-15. Fault-plane solution for Borrego Mountain earthquake. L2 norm estimate with 6.4-percent dipole and 93.6-percent double couple. One data point has been artificially amplified by a factor-of-10.
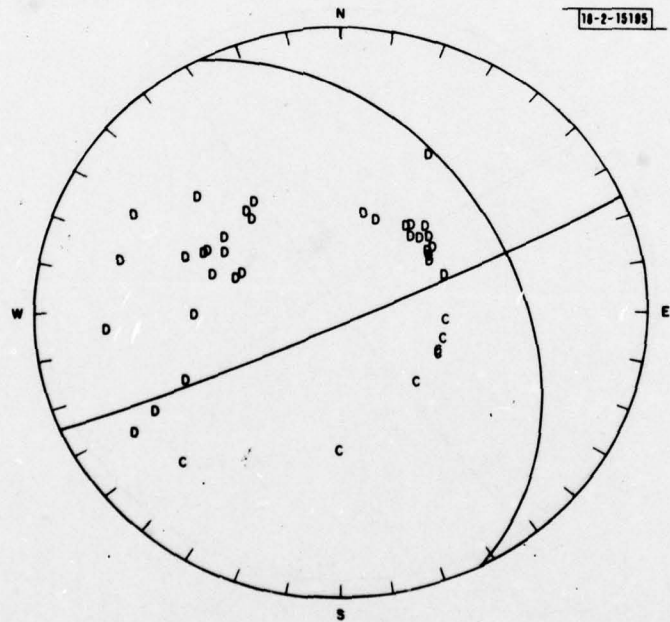
Fig. II-16. Fault-plane solution for Fiji-Tonga earthquake, 9 October 1967. L1 norm estimate with 17.7-percent monopole, 23.8-percent dipole, and 58.5-percent double couple; 28 LP amplitudes and 13 LP polarities used.
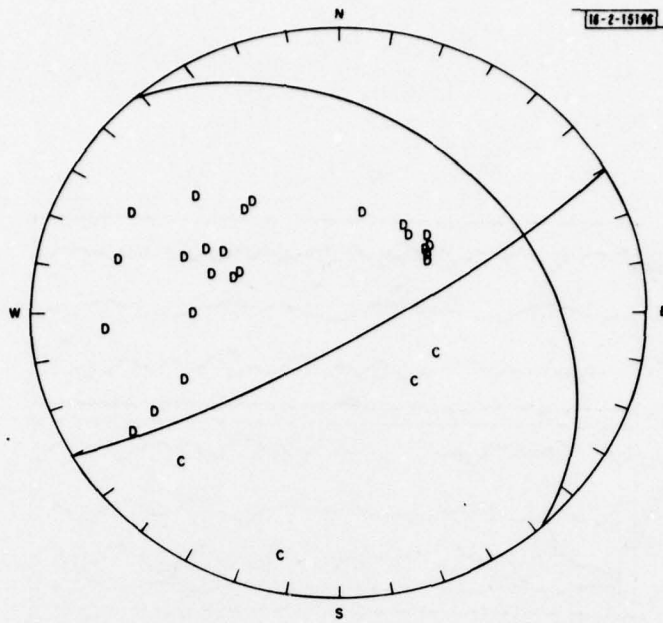
Fig. II-17. Fault-plane solution for Fiji-Tonga earthquake. L2 norm estimate with 4.5-percent monopole, 7.0-percent dipole, and 87.5-percent double couple; 28 LP amplitudes used.
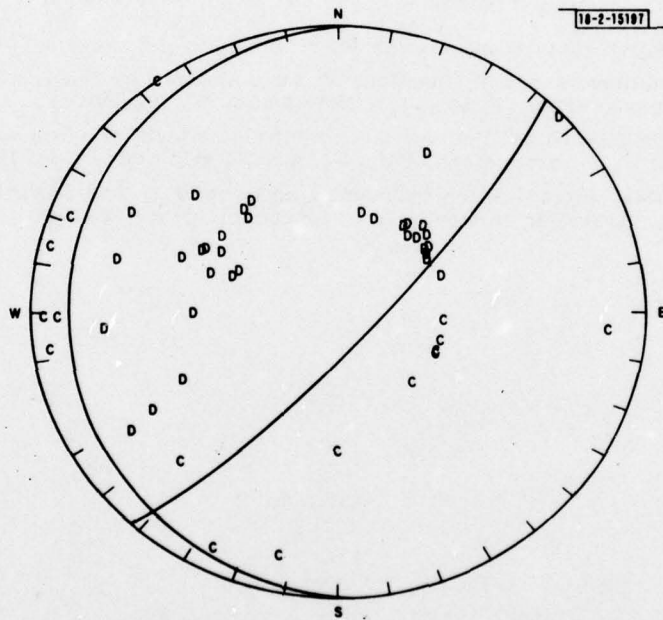
Fig. II-18. Fault-plane solution for Fiji-Tonga earthquake. L1 norm estimate with 8.9-percent monopole, 13.9-percent dipole, and 77.2-percent double couple; 28 LP amplitudes, 13 LP polarities, and 9 SP polarities used.
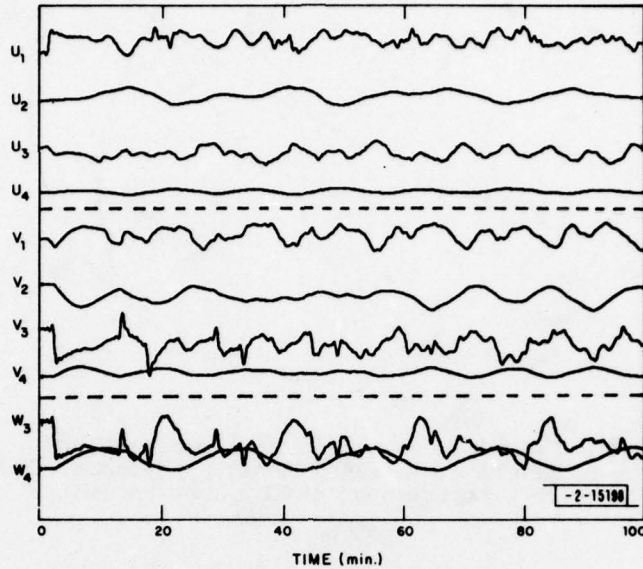
Fig. II-19. Excitation functions U, V, and W for source depth of 650 km and angular order l = 4. Elastic earth model 1066B (Ref. 9), anelastic model FSQMK (Refs. 5 and 11). Modes from $_0S_4$ to $_{60}S_4$ were used to construct functions U and V; functions W were obtained by superposition of toroidal modes from $_0T_4$ to $_{21}T_4$. Note that on U_1 SP pulses are equivalent to PKIKP and pPKIKP and their multiple reflections — ScS and sScS on V_3 and W_3. Abrupt steps in U_1, V_3, and W_3 at times of roughly 1 and 2 min. after origin time correspond to arrivals of P- and S-waves, respectively, traveling vertically from source to surface of earth.

40
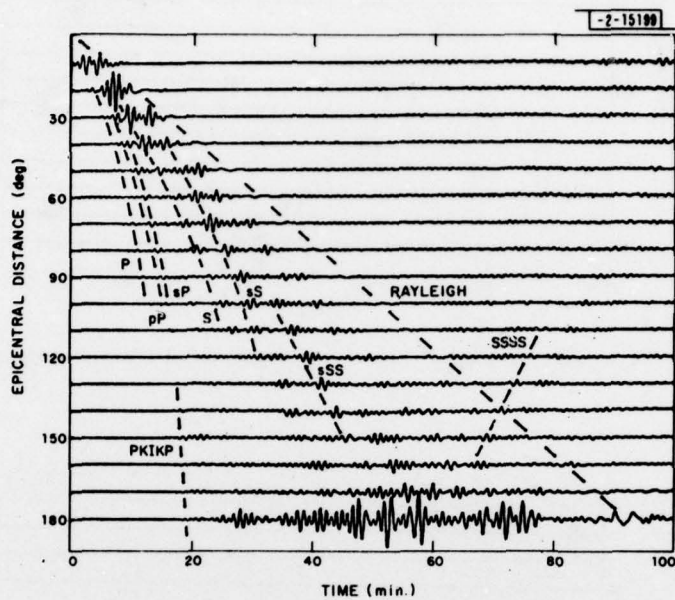
Fig. II-20. Record sections of synthetic seismograms for vertical component, recorded by a simulated WWSSN instrument, for source depth of 650 km. Double-couple source mechanism determined by Mendiguren[12] for Colombian earthquake of 31 July 1970. Azimuth for all receivers is 0°. Note amplification of signal due to convergence of waves at 180°.
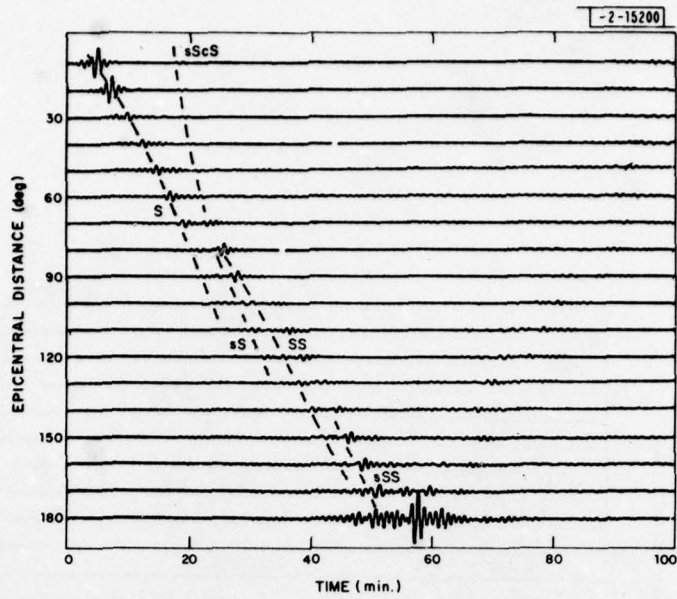
Fig. II-21. Same as Fig. II-20 but for longitudinal (radial) component.
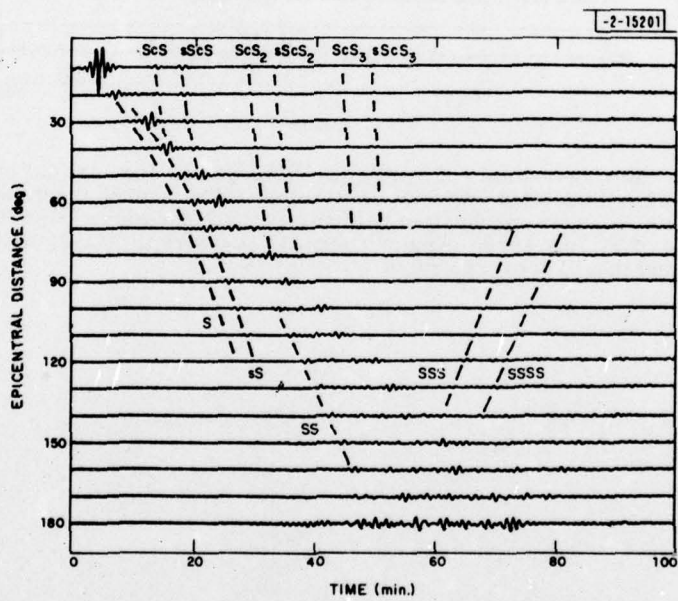
Fig. II-22. Same as Fig. II-20 but for transverse component.

III. MISCELLANEOUS STUDIES

A. DETECTION CHARACTERISTICS OF THE SRO STATIONS

Several published reports[1,2] have described the performance of the Seismic Research Observatories (SROs). We present here an updated evaluation of detection performance, including that for four new sites (ZOBO, Bolivia; MAJO, Japan; KAAO, Afghanistan; and CHTO, Thailand). For the first 86 days of 1978, we have compared the short-period (SP) detections recorded at ten SRO/ASRO stations with the SDAC Bulletin; both these sources were accessed via the Datacomputer.

For each station, theoretical P and PkP arrival times were computed for all the events in the SDAC Bulletin. An event was assumed to have been detected if this arrival time lay within the time interval saved. Since for each SRO/ASRO detection the data are saved starting 10 to 30 sec prior to the detection time, and for several tens of seconds afterward, small errors in origin and travel times and location will not affect the results. To account for subsequent detection of later phases from the same event, we have also included as "associated" all detections within the subsequent 15 min. of a detected P/PkP arrival. Such secondary-phase associations accounted for 25 to 50 percent of all associated detections.

In Table III-1 we give, for each station studied, the time period used (station downtimes were not included), the percentage of the total time interval for which the detector was on, the

<table>
<tr><td colspan="6" align="center">TABLE III-1
DETECTION CHARACTERISTICS OF TEN SRO/ASRO STATIONS</td></tr>
<tr><td>Station</td><td>Period*
Studied</td><td>Percent of Time
Detector On</td><td>Number
of Detections</td><td>Associated†
(percent)</td><td>50-Percent
Detection Threshold‡
(m_b)</td></tr>
<tr><td>ANMO</td><td>1 – 86</td><td>3.9</td><td>2058</td><td>50.0</td><td>4.6</td></tr>
<tr><td>CHTO</td><td>1 – 86</td><td>7.0</td><td>4692</td><td>35.3</td><td>4.4</td></tr>
<tr><td>CTAO</td><td>1 – 86</td><td>3.1</td><td>1606</td><td>24.9</td><td>5.2</td></tr>
<tr><td>GUMO</td><td>1 – 86</td><td>9.2</td><td>5530</td><td>7.6</td><td>5.8</td></tr>
<tr><td>KAAO</td><td>1 – 86</td><td>9.2</td><td>3500</td><td>32.4</td><td>4.4</td></tr>
<tr><td>MAIO</td><td>60 – 86</td><td>9.1</td><td>687</td><td>66.0</td><td>4.5</td></tr>
<tr><td>MAJO</td><td>1 – 61</td><td>2.9</td><td>630</td><td>41.6</td><td>5.0</td></tr>
<tr><td>NWAO</td><td>1 – 85</td><td>3.5</td><td>709</td><td>30.6</td><td>5.7</td></tr>
<tr><td>TATO</td><td>1 – 85</td><td>2.4</td><td>1448</td><td>9.3</td><td>5.8</td></tr>
<tr><td>ZOBO</td><td>1 – 41</td><td>5.3</td><td>1200</td><td>20.8</td><td>4.8</td></tr>
</table>

* Expressed as Julian days (1978).

† See text for association scheme.

‡ Estimated from data shown in Figs. III-1(a) through (j).

number of detections, and the percentage of detections that were associated according to the scheme described above. As has been noted previously,[1,2] the detection performance of island stations GUMO and TATO appear to be very poor.

At each station we have evaluated the detection characteristics for events within a distance of 100°: the results are shown in Figs. III-1(a) through (j). In the last column of Table III-1 we give the approximate 50-percent detection threshold inferred from the data shown in these figures. Stations CHTO, KAAO, MAIO, and ANMO have the lowest detection thresholds, all below m_b 4.6. Note that GUMO, with more total detections than CHTO, has an extremely high detection threshold at m_b 5.8 compared with 4.4 for the latter: a very high proportion of the detections for GUMO (and also NWAO and TATO) are probably false alarms.

In an attempt to determine the "true" false-alarm rate, we have retrieved from the Data-computer the 236 SP seismograms corresponding to detections at ANMO from 20-31 December 1976. Using the associated scheme described above, only 70 of these could be linked to P/PkP arrivals, and 16 to secondary phases of these events; the 50-percent detection threshold for this time interval was ~4.5, which is close to that determined for the longer time interval [see Fig. III-1(a) and Table III-1].

Each of the SP detections was bandpass filtered over the frequency band 0.5 to 2.0 Hz to simulate the data run through the on-site detection processor.[2] We studied each of the 150 un-associated detections to see whether an analyst would have picked a phase in the detected interval. Four of the "detections" were, in fact, saved calibration pulses. Of the remaining 146 detections, inspection of the data showed that an analyst as unexperienced as this author would have picked 101 as clear seismic phase arrivals. For the remaining 45, it was difficult to see exactly what triggered the detection algorithm: this "false-alarm" rate of 19 percent is quite acceptable, however, and might even be considered too low for optimum detector performance.

For the 101 phase arrivals selected above, we returned to the raw (i.e., not bandpass filtered) SP data and re-inspected the traces. From their high frequency character (dominant frequency >2.5 Hz), 57 of these could be reasonably assumed to result from local events at distances of probably less than 10°. Such a distance from Albuquerque includes Southern California and the northern portion of the Gulf of California and Baja California. No local Bulletin for this region was available to verify this hypothesis.

With the exception of Australian stations NWAO and CTAO, all the SRO/ASRO stations are situated within, or close to, regions of probably higher seismic activity than ANMO. This will certainly be true for such stations as CHTO, GUMO, KAAO, MAIO, MAJO, and TATO. It is thus likely that the "true" false-alarm rates, i.e., percentage of detections which would not be picked by an analyst, are extremely low. A possible exception to this is the notorious performance of GUMO, at which the detector was switched on for 9.2 percent of an 86-day interval, but which detected only 16 percent of events of $m_b > 4.5$ at distances of less than 100°!

<div align="right">R. G. North</div>

B. A MULTIPLE-FREQUENCY BAND SHORT-PERIOD SIGNAL DETECTOR

In Sec. A above, we described the results of an evaluation of the detection performance of the SRO/ASRO stations. It was noted there that the false-alarm rate of the detector presently operating at the SRO sites was probably at least as low as 25 percent, though many of the detections, particularly those which could be recognized as being from close events by their

<div align="center">44</div>

frequency content, could not be associated with Bulletin events. We present here the results of an attempt to separate local and teleseismic events during the detection process.

Much research has been carried out in the past on the design of signal detectors suitable for seismic data. Most of these, however, have been primarily designed for seismic arrays rather than the single stations which are now superseding the arrays. All suggested detectors measure a particular property (such as power) continuously, and compare its instantaneous value with a long-term average of this property, often described simply by its statistical characteristics such as mean and variance. This long-term average is either continuously or intermittently measured, and a detection is declared when the short-term instantaneous value of the detector output exceeds that of the long term by more than a chosen threshold.

The present SRO detector operates on a narrowly (0.5 to 2.0 Hz) bandpass-filtered portion of the SP filtered output of the SRO instrument, and measures power averaged over 1-sec samples. Since only detections are saved, we are generally unable to properly evaluate the performance of the detector since we do not, for example, know what the character of the "missed" signals (as predicted by Bulletin location, for example) was and precisely why the detector failed. However, during the latter half of 1977, a SRO instrument at ANMO (Albuquerque) was intermittently run in a broadband mode, i.e., without separation into SP and LP passbands. We have selected for study a $5\frac{1}{2}$-hr segment of this continuously recorded (20-Hz) broadband data, starting at 18:17:51 on 23 December 1977.

Previous attempts[3] to utilize variations in spectral power as a detection method have not been shown to be demonstrably superior to the traditional technique of power measurement on data which have, as in the case of the SRO detector, been bandpass filtered over frequencies assumed to be of seismic interest. Often, such spectral techniques are computationally prohibitive, such as those which calculate spectra of moving or adjacent cells[3] of data. However, a numerically efficient scheme has been derived[4] for iteratively computing spectra, and we apply here a modification of this technique. The latter computed spectral power at a number of frequencies, and used power averaged over all frequencies as a detection characteristic. In order not only to detect events but also to decide whether, from their frequency content, they are local or teleseismic, we have determined spectral power at 0.5 to 5.0 Hz in 0.5-Hz steps and defined high (HF) and low (LF) powers as

$$LF = \frac{1}{4} [P(0.5) + P(1.0) + P(1.5) + P(2.0)]$$

$$HF = \frac{1}{4} [P(2.5) + P(3.0) + P(3.5) + P(4.0)]$$

where $P(x)$ is the spectral power at the frequency (x) in hertz. A short-term average-power spectrum was determined from the current 60 samples (3 sec) of data, averaged over the previous 60 determinations, and the long-term power spectrum from the preceding 600 samples of data, again averaged over 60 samples. Details of the computation scheme may be found in Ref. 4. A detection was declared when the ratio of either HF or LF to its long-term average exceeded a certain threshold T. For each detection, the maximum power in HF and LF was measured. Figure III-2 shows the amount of total detector on-time as a function of threshold T. The detector has been run on the broadband seismometer output, not on a filtered version of the SP output channel.

During the time interval studied, the on-site detector at ANMO made 10 detections, totaling 2500 sec or 12.9 percent of the total time interval. Of these, 7 could be associated with

SDAC Bulletin events and 3 could be readily seen to be local events from their high-frequency content. At T = 3.0, eleven individual detections were made by the algorithm described above. Of these, 8 corresponded to the ANMO detections: the two events missed were unfortunately teleseismic Bulletin events. At lower values of the threshold T, the false-alarm rate was unacceptably high.

In Fig. III-3 we show maximum values of HF and LF for each of the detections. Detections marked (A) were also made by the on-site detector. Note that the 5 teleseismic events all have LF/HF ratios > 1, and that the 3 local events have (LF/HF) < 1. Although the detection performance of the algorithm is rather poor, it appears to adequately discriminate between teleseismic and local events. Similar results could, of course, have been obtained by running a power detector of the SRO type on the outputs of two bandpass filters corresponding to the frequency ranges used in the HF and LF determinations. However, we could have evaluated power spectra at a variety of other frequency bands (including, since we are using broadband data, one corresponding to surface-wave frequencies) with little more effort, and then the iterative spectral power scheme would be considerably faster computationally than a series of corresponding bandpass filters on such a large volume of data. Such a technique also has applications to the computation of spectral ratios as used in an explosion-earthquake discrimination contest. We propose to further evaluate the above combined detection-discrimination scheme.

<div align="right">R. G. North</div>

C. MEASUREMENT OF m_b USING SRO DATA

We have commenced a study of the estimation of m_b using high-quality SP waveforms from SRO and ASRO stations. Several important questions need to be answered. First, how should these waveforms be used in the overall estimation of m_b for an event? Second, what are the characteristics of the SP waveforms observed at these sites from different source areas? And third, how should we approach magnitude corrections for this network? We report here some preliminary observations, based on a rather small data set.

Figures III-4 and III-5 show waveforms observed at 5 stations from two events in the Aleutian Islands (event details are listed in the figure captions). Notice that Charters Towers (CTAO), Kabul (KAAO), and Matsushiro (MAJO) are ASRO sites, while the remainder are SROs. The waveforms are shown roughly equal in size, but notice that there is a large variation in the amplitude scale. The approximate amplitude of the largest peak-to-peak value in the first few cycles is indicated in millimicrons on each waveform. The traditional m_b value, including distance and instrument-response corrections, is also shown for each waveform. The mean SRO m_b value for each event is close to that quoted in the SDAC Weekly Event Summary (within 0.1 or 0.2 m_b units). Also, the standard deviation of the observations is 0.3 to 0.4, which is close to that usually observed.[5]

There are clearly substantial variations in both amplitude and shape of waveform. In the case of the Andreanoff Islands event (Fig. III-4), there is a substantial buildup of energy (in some cases by an order-of-magnitude) over the first 20 to 30 sec. A pP phase appears to occur at 7 to 8 sec after the P-wave onset, but this seems generally larger than the P phase at all azimuths, so positive identification is not easy. The Fox Islands event (Fig. III-5) is much more impulsive at all azimuths.

In both cases, it is interesting to note that large amplitudes appear to correlate with short dominant periods. In particular, Kabul (KAAO), Matsushiro (MAJO), and Chiengmai (CHTO) have dominant periods of close to 1 sec, and larger amplitudes, while the remaining stations have dominant periods of up to 2 sec, and much lower amplitudes.

A very large difference is noted between Kabul (KAAO) and Mashhad (MAIO). These stations are relatively close together, and at a similar azimuth for events in the Aleutian Islands, yet the station m_b at Kabul is between 0.6 and 1.1 m_b units higher than Mashhad for all events studied in the Aleutians to date. The general pattern of amplitudes found for these events is repeated for other events in the Aleutians. Figure III-6 shows similar data for an event in the Kuril Islands. Mashhad is less anomalous, but large m_b values are still observed at KAAO and CHTO.

Since Figs. III-4 through III-6 are typical of events in the Aleutians and Kurils, it would appear that much of the variation in m_b across the network can be attributed to systematic bias, rather than random scattering processes. North[6] was unable to demonstrate a dependence of receiver bias on source region. The present results suggest a substantial bias (perhaps approaching one magnitude unit for the Kabul-Mashhad station pair) which is consistent over a source region of the size of the Aleutian arc. Removal of this bias could result in very much smaller estimates of the standard deviation of the random scattering component.

Research is continuing into the further definition of these source region dependent station biases.

<div align="right">

J. C. Johnston
M. A. Chinnery

</div>

D. MANTLE LOVE-WAVE DISPERSION FROM SRO DATA

Surface waves at periods in excess of 100 sec are an important source of information on upper-mantle structure, since energy at their wavelengths (400 to at least 2000 km) is mainly concentrated in this region. In particular, they are of great use in resolving whether continent-ocean, and other, differences extend to greater depths than shown by simpler crust-uppermost mantle models deduced from shorter-period surface-wave dispersion. However, such studies have previously been limited to recordings of the rare great ($M_s > 8.0$) earthquakes. The broad dynamic range of the SRO instrumentation permits detection and analysis of mantle waves from earthquakes as small as $M_s = 6.5$; these are much more frequent (~15/year for 1976 to 1978). Figure III-7 shows an example of mantle Love (G) waves recorded at SNZO (New Zealand, $\Delta = 78°$) from an $M_s = 7.1$ earthquake occurring on 26 August 1977 in the Southwest Atlantic Ocean. The seismogram shown starts 1000 sec after the event origin time and is of duration ~7 hr. The data have been low-pass filtered with a forward and reverse (phase-free) Butterworth filter with a 6-dB point at 0.01 Hz. The second pass (G2) of the Love wave is the largest arrival; subsequent passes of G3 through G6 are clearly visible. Such high-quality data are ideally suited to a study of mantle-wave dispersion and Q.

We have analyzed SRO/ASRO recordings of five earthquakes occurring during August to December 1977. The event parameters and stations used are given in Table III-2 and the circumferential paths on a mercator projection are shown in Fig. III-8. At present, we have restricted ourselves to G waves recorded on the transverse (after rotation into epicenter azimuth) component; the extremely flat group-velocity curve for Love waves at mantle-wave periods produces short-pulse-like arrivals as shown in Fig. III-7. Each transverse component record was

TABLE III-2
EVENT-STATION PAIRS USED

Date (1977)	Origin Time	Latitude	Longitude	Region	M_s	Stations Used
19 August	06:08:55.2	11.1°S	118.5°E	Sumbawa	7.9	ANMO, SNZO, CTAO, ZOBO, CHTO
10 October	11:53:53.6	25.9°S	175.4°W	Tonga	7.2	ANMO, GUMO, TATO, ZOBO, NWAO, CTAO, CHTO
1 October	17:26:40.4	27.9°S	173.1°E	Kermadec	6.7	ANMO, GUMO, MAIO, TATO, NWAO, CTAO, CHTO
23 November	09:26:24.7	31.0°S	67.8°W	Argentina	7.4	ANMO, GUMO, MAIO, CTAO, KAAO, SNZO
28 December	02:45:36.7	16.7°N	40.3°E	Red Sea	6.6	ANMO, GUMO, MAIO, TATO, ZOBO, NWAO, CTAO, KAAO, CHTO, SNZO

low-pass filtered and reduced to a 16-sec sampling rate. Subsequent passes of the G wave (G2 through G4) were windowed between group velocities of 4.25 to 4.50 km/sec. We measured phase velocities C for each record using the classical formula[7]

$$C(T) = \frac{\delta \Delta}{[\delta t + T(\frac{\delta \phi}{2\pi} + N + \frac{1}{2})]}$$

from pairs (G2, G4) and (G3, G5), where $\delta \Delta$ is the length of the circumferential path (corrected for ellipticity), δt is the difference in window start times, and $\delta \phi$ is the phase difference at the chosen period T. The factor of $\frac{1}{2}$ accounts for the polar phase shift, and N is an integer chosen to provide a smooth fit to free oscillation data at the longer periods. Such a differential measurement eliminates both source and instrumental effects. The phase difference $\delta \phi$ was determined from the cross-correlogram of the windowed seismogram, as this has been shown to provide better results than differences of individual phase spectra.[8]

For each seismogram, phase velocity was determined for (G4, G2) and (G5, G3) pairs, thus providing a good check upon the accuracy of the results over a single path. We rejected paths for which the phase velocities determined from (G2, G4) and (G3, G5) differed by more than 0.01 km/sec. In Fig. III-9(a) we show the results obtained for the paths given in Table III-2 and Fig. III-8. The results are shown as deviations from the dispersion predicted by the oceanic model 5.08M (Ref. 9). Each datum is the mean of a number (given) of observation. The bars indicate ±1 standard deviation. Shown below this [Fig. III-9(b)], for comparison, are results obtained[10] from recordings of the great Alaskan and Kuril earthquakes of 1964 and 1953, respectively, expressed in the same manner. We do not attach any significance to the deviation from 5.08M, but wish rather to point out the small standard deviation obtained using SRO data from events as small as $M_s = 6.6$. We propose to continue this study (some 45 events of $M_s > 6.5$ have occurred during 1976–1978) for many more paths, including Rayleigh-wave data.

We believe that enough results can be obtained to permit a detailed regionalization of phase delays over several hundred paths in order to contour phase velocity at a variety of periods and (by implication) depths within the upper mantle.

R. G. North

E. LITHOSPHERIC STRUCTURE OF THE WALVIS RIDGE FROM RAYLEIGH-WAVE DISPERSION

The Walvis ridge is a linear topographic feature located in the South Atlantic Ocean (see Fig. III-10) which appears to have no natural seismicity.[11] The origin of an aseismic ridge like the Walvis ridge is usually attributed to hot-spot plume activity at mid-ocean spreading centers.[12] While their kinematic behavior agrees with plate tectonic theory, the deep structure of aseismic ridges is poorly understood. Only one reversed marine refraction line exists sampling upper-mantle depths. The interpretation indicates a 16-km-thick oceanic crust over a low-velocity (V_p = 7.93 km/sec) mantle.[13] The small free-air gravity anomaly across aseismic ridges has been used to infer Airy-type crustal thickening.[14,15] To provide additional constraints on the structure of aseismic ridges, we present here the results from Rayleigh-wave group-velocity dispersion analyses. Unfortunately, due to geographical limitations, only two suitable South Atlantic events were found having nearly identical epicenters (19 April 1968). So, our results are limited to just the Walvis ridge.

The long-period vertical seismograms from WWSSN stations SDB and WIN were digitized, and group velocities were calculated by the multiple-filter technique.[16] The instrument group delay was removed by the usual method.[17,18] Since the station distribution in the South Atlantic is poor, no fault-plane solutions could be found and no phase velocities could be measured. The resulting Rayleigh-wave group-velocity dispersion curves for the on-ridge (SDB) and off-ridge (WIN) crustal paths are compared with the 20- to 50-million-year-old pure-path result of Forsyth[19] in Fig. III-11.

Significant differences exist between the on-ridge and off-ridge dispersion, and between both of these and that for a normal oceanic lithosphere. Reasonable values of epicenter mislocation, lithospheric anisotropy, and lateral refraction cannot explain the differences. Station timing was checked by measuring the P arrival time on the SP record, and was found not to exceed 1 sec. This implies to us that the anomalous dispersion is real, and that a deficiency of high-velocity material exists under the Walvis ridge.

The dispersion data were inverted for the shear-wave velocity structure using the formalism of Wiggins[20] as adapted by Rodi et al.[21] Since inverting group-velocity dispersion is a highly nonlinear problem and also because phase-velocity information was not available to constrain the inversion, we searched for the smallest changes from a standard model that fit the data. The actual starting model we used was that of Forsyth.[19] Final models for both South Atlantic paths are compared with the 20- to 50-million-year-old pure-path result in Fig. III-12. The resolving kernels for both models are compact, so the parameters shown are required by the data. Prominent features of the on-ridge model are a 12.5- ± 3-km-thick crust and a low-velocity (V_s = 4.26 km/sec) upper-mantle lid to depths of 40 to 50 km. The off-ridge model has a normal oceanic crustal structure with a 4.40-km/sec upper mantle to depths of 50 km. No significant differences from normal oceanic lithosphere exist below 50 km in either model.

Rayleigh waves are sensitive to compressional-wave velocity and density as well as to shear-wave velocity. In order to evaluate the effect of neglecting these variables, the pertinent partial

49

derivatives of group velocity were investigated. Compressional-wave velocity has no significant effect below the upper crust and therefore can be safely neglected. Density can affect the results into the upper mantle and must be taken into account. Perturbing the upper-mantle density from 3.40 to 3.20 gm/cc produces a 0.06-km/sec rise in the upper-mantle lid velocity and a very slight reduction below this depth. In either case, the resulting shear velocities shown in Fig. III-12 are significantly lower than those of normal oceanic lithosphere.

The velocities presented here are averages for the entire paths shown in Fig. III-10. The differences between the on-ridge and off-ridge results may be due to the Rayleigh waves traversing a path which is half over the ridge and half over the, presumably normal, Cape Basin. The available data are not capable of distinguishing this effect.

Possible explanations for the low-velocity mantle in our model include partial melting and compositional changes. The former can be eliminated on the basis of the measured heat flow, which is only slightly higher than that in the surrounding ocean basins.[22] The second possibility is attractive due to the unique isotopic composition of Walvis ridge volcanics[23,24] which could indicate an anomalous source region. Iron enrichment in the mantle can easily produce the required reduction in shear velocity with no large density change.[25] Further data, preferably compressional-wave velocity measurements, are required to settle the issue.

A. D. Chave[†]
J. D. Phillips
D. W. McCowan

F. PHASE VELOCITY OF L_g IN NORTH AMERICA

Maximum-likelihood-array processing[26] has been used to determine the phase velocity of the vertical component of L_g for several North American continental paths. Table III-3 lists

TABLE III-3 **ARRAY ANALYSIS EVENT PARAMETERS**							
Event	Origin Time	Array	Δ (deg)	V (Group) (km/sec)	V (Phase) (km/sec)	ΔV (Phase) (km/sec)	Frequency (Hz)
GAS	10 December 1967 19:30:00.1	LASA	10.0	3.5	4.4	0.18	1.1
MINN	9 July 1975 14:54:16.3	YKC	20.0	3.5	4.5	0.05	1.0
N.C.	30 November 1973 07:48:38.7	LASA	19.7	3.5	3.9	0.08	1.1
Q.C.	15 July 1971 00:24:03.1	LASA	19.2	3.5	4.6	0.11	0.9

[†] Woods Hole Oceanographic Institution, Woods Hole, Massachusetts 02543, and Department of Earth and Planetary Sciences, M.I.T., Cambridge, Massachusetts 02139.

the events used in this study and the corresponding measured phase velocity and precision obtained at the listed array. The LASA B2 subarray was used for the Gasbuggy (GAS) explosion and the North Carolina (N.C.) and Queen Charlotte Island (Q.C.) earthquakes. The Yellowknife (YKC) array was used to measure the phase velocity of the Minnesota (MINN) earthquake. In each case, the measurement was made at the time corresponding to an L_g group velocity of 3.5 km/sec, and at a frequency near 1 Hz. For every event except GAS, the L_g arrival was well above the coda level with its maximum amplitude near the above group velocity of 3.5 km/sec. At the time corresponding to that group velocity for the GAS data, there was no discernible change in the coda level; however, the array processing clearly indicated the L_g arrival. The precision of the measurements was determined by converting the 3-dB half-width of the corresponding wavenumber power spectrum peak to velocity. The results are shown in Fig. III-13. In the previous SATS,[27] the same measurement was made for a Western Russia event at a subarray of NORSAR. For those data at the same 3.5-km/sec group-velocity point, the phase velocity was 4.1 km/sec.

As has been noted by others,[27-29] these measurements are consistent with the behavior of higher-mode Rayleigh waves whose main lobe of elastic energy is confined to the middle portion of the crust. However, the phase velocities at 1 Hz are significantly higher than those that would be obtained for a J-B model of the crust and upper mantle unless modified by a low-shear-velocity zone (LVZ) in the upper mantle overlaid by a high (4.8-km/sec or more) shear-velocity lid.[29] These results support the existence of a LVZ with a high-velocity lid in the most stable of continental regions (the Baltic and Canadian Shields), perhaps implying that a well-defined lithosphere-asthenosphere boundary persists continuously around the globe. Our data also tend to substantiate that these waves propagate coherently along apparently high-Q paths over tectonic environments ranging from Shield to Basin and Range regimes. On this basis, coherent processing of the phase should aid discrimination and detection capability for continental source-receiver paths.

<div align="right">

T. E. Landers
T. J. Fitch

</div>

REFERENCES

1. A. C. Strauss, "Preliminary Evaluation of the Seismic Research Observatories," Texas Instruments Report ALEX(01)-TR-76-02 (1976).

2. A. C. Strauss and L. C. Weltman, "Continuation of the Seismic Research Observatories Evaluation," Texas Instruments Report ALEX(01)-TR-77-02 (1977).

3. M. J. Shensa, "The Deflection Detector — Its Theory and Evaluation on Short-Period Seismic Data," Texas Instruments Report ALEX(01)-TR-77-03 (1977).

4. Seismic Discrimination Semiannual Technical Summary, Lincoln Laboratory, M.I.T. (31 December 1973), DDC AD-777151/2.

5. D. Von Seggern, "Joint Magnitude Determination and Analysis of Variance for Explosion Magnitude Estimates," Bull. Seismol. Soc. Am. 63, 827-845 (1973).

6. R. G. North, "Station Magnitude Bias — Its Determination, Causes, and Effects," Technical Note 1977-24, Lincoln Laboratory, M.I.T. (29 April 1977), DDC AD-A041643/8.

7. M. N. Toksöz and A. Ben-Menahem, "Phase Velocities of Long Period Surface Waves and Structure of the Upper Mantle," J. Geophys. Res. 71, 1649 (1966).

8. M. Landisman, A. Dziewonski, and Y. Sato, "Recent Improvements in the Analysis of Surface Wave Observations," Geophys. J. R. Astr. Soc. 17, 369 (1969).

9. F. Press, "Regionalised Earth Models," J. Geophys. Res. 75, 6575 (1970).

10. H. Kanamori, "Velocity and Q of Mantle Waves," Phys. Earth Planet. Int. 2, 259 (1970).

11. C. Stover, "Seismicity of the South Atlantic Ocean," J. Geophys. Res. 73, 3807 (1968).

12. J. T. Wilson, "Evidence from Islands on the Spreading of Ocean Floors," Nature 197, 536 (1963).

13. S. T. Cutler, "Geophysical Investigation of the Nazca Ridge," M.S. Thesis, University of Hawaii, Honolulu (1977).

14. M. H. P. Bott, C. W. A. Browitt, and A. P. Stacey, "The Deep Structure of the Iceland-Faeroe Ridge," Mar. Geophys. Res. 1, 328 (1971).

15. J. Goslin and J. C. Sibuet, "Geophysical Study of the Eastern Walvis Ridge, South Atlantic: Deep Structure," Geophys. Soc. Am. Bull. 86, 1713 (1975).

16. A. Dziewonski, S. Block, and M. Landisman, "A Technique for the Analysis of Transient Seismic Signals," Bull. Seismol. Soc. Am. 59, 427 (1969).

17. T. Hagiwara, "A Note on the Theory of the Electromagnetic Seismograph," Bull. Earthquake Res. Inst. 36, 139 (1958).

18. J. N. Brune, "Correction of Initial Phase Measurements for the Southeast Alaska Earthquake of July 10, 1958 and for Certain Nuclear Explosions," J. Geophys. Res. 67, 3643 (1962).

19. D. W. Forsyth, "Anisotropy and the Structural Evolution of the Oceanic Upper Mantle," Geophys. J. R. Astr. Soc. 43, 103 (1975).

20. R. Wiggins, "The General Linear Inverse Problem: Implications of Surface Waves and Free Oscillations for Earth Structure," Rev. Geophys. 10, 251 (1972).

21. W. Rodi, P. Glover, T. M. C. Li, and S. S. Alexander, "A Fast, Accurate Method for Computing Group-Velocity Partial Derivatives for Rayleigh and Love Modes," Bull. Seismol. Soc. Am. 65, 1105 (1975).

22. T. C. Lee and R. P. Von Herzen, "A Composite Trans-Atlantic Heat Flow Profile Between 20°S. and 35°S.," Earth Planet. Sci. Lett. 35, 123 (1977).

23. P. W. Gast, G. R. Tilton, and S. Hedge, "Isotopic Composition of Lead and Strontium from Ascension and Gough Islands," Science 145, 1181 (1964).

24. V. Oversby and P. W. Gast, "Isotopic Composition of Lead from Oceanic Islands," J. Geophys. Res. 75, 2097 (1970).

25. F. Birch, "Density and Composition of the Upper Mantle: First Approximation as an Olivine Layer," in The Earth's Crust and Upper Mantle, P. J. Hart, Ed. (American Geophysical Union, Washington, D.C., 1969).

26. J. Capon, "High-Resolution Frequency-Wavenumber Spectrum Analysis," Proc. IEEE 57, 1408-1418 (1969), DDC AD-696880.

27. Seismic Discrimination Semiannual Technical Summary, Lincoln Laboratory, M.I.T. (31 March 1978), DDC AD-A057279.

28. L. Knopoff et al., "Evaluation of L_g as a Discriminant Among Different Continental Crustal Structures," Geophys. J. R. Astr. Soc. 39, 41 (1974).

29. G. F. Panza and G. Calcagnile, "L_g, L_i and R_g from Rayleigh Modes," Geophys. J. R. Astr. Soc. 40, 475 (1975).
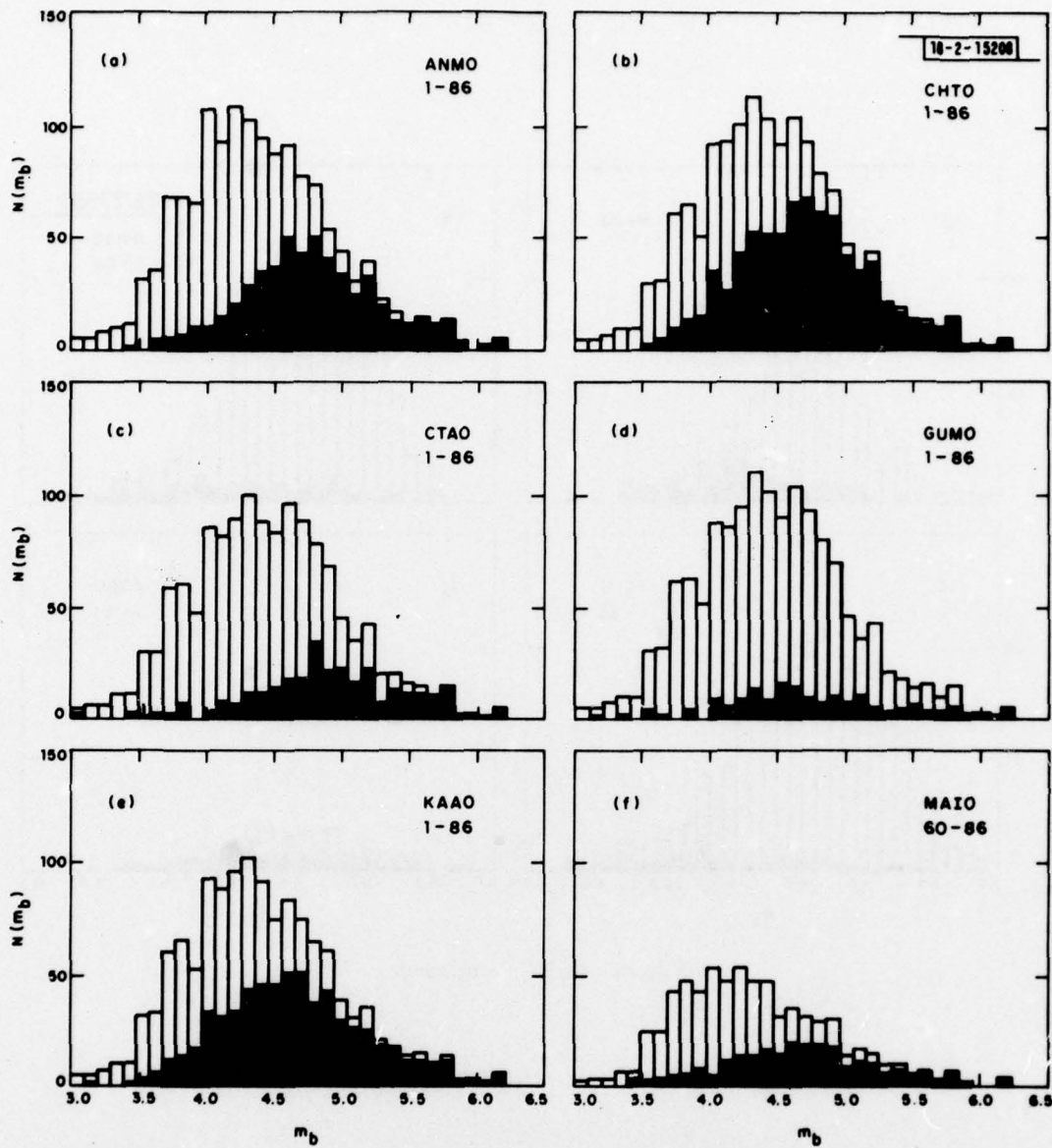
Fig. III-1(a-j).   Detection performance of ten SRO/ASRO stations. m_b-frequency statistics for events within 100° (source: SDAC Bulletin).   Black portion indicates detection, white indicates nondetection.   Time interval studied (Julian date, 1978) is given for each station.
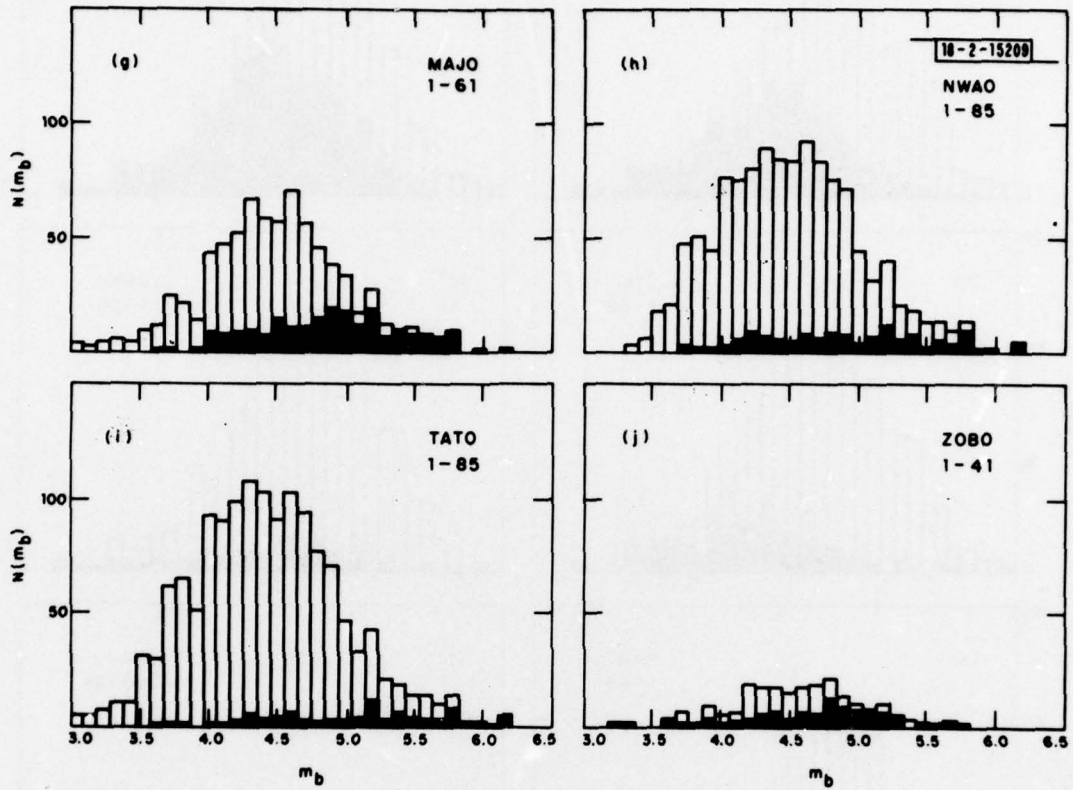
Fig. III-1(a-j). Continued.

54

Fig. III-2. Detector on-time as a function of detection threshold T. Lowest false-alarm rate consistent with best performance obtained with T = 3.0.
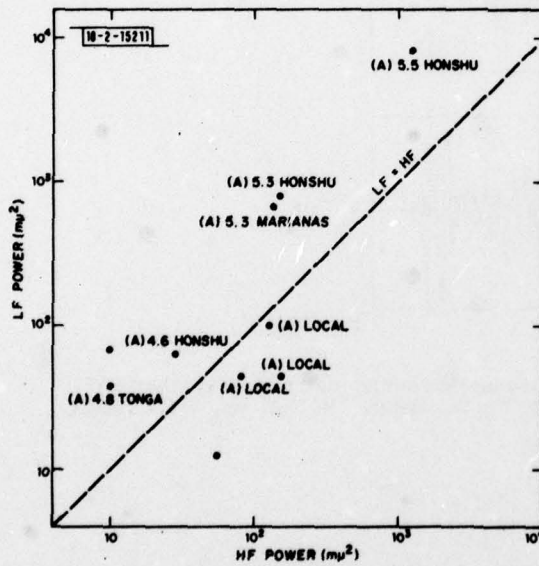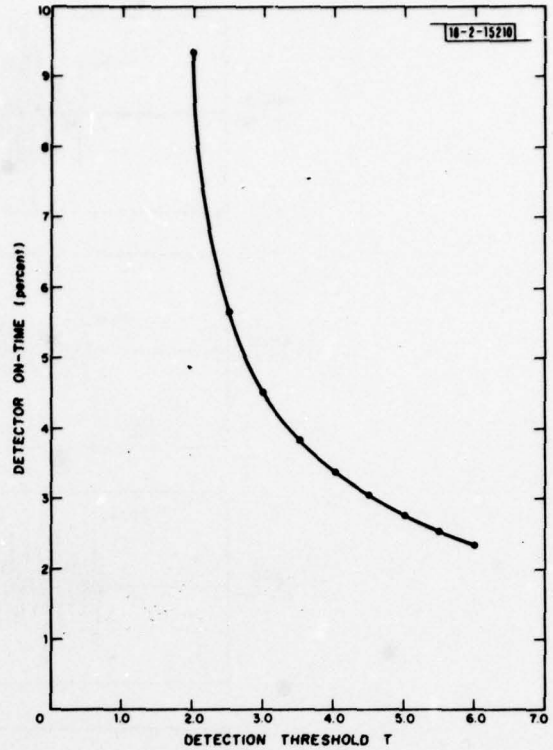
Fig. III-3. High (HF) and low (LF) frequency spectral power averages measured at peak power (larger of HF and LF) for each of 11 detections obtained. Detections also made by SRO detector are designated (A) — magnitude and location of associated detections are also given. Note that teleseismic arrivals lie above line of HF = LF.

55
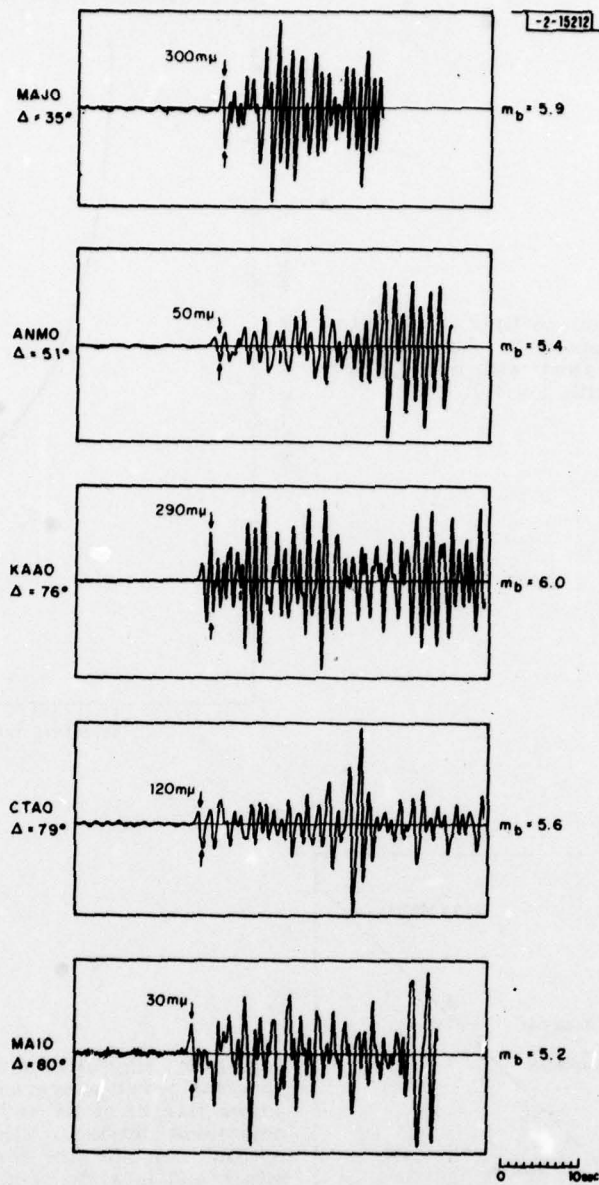
Fig. III-4. Event parameters. Region: Andreanoff Islands; date: 4 November 1977; origin time: 9:53:4; location: 51.71°N, 176.05°W; depth: 95 km, m_b = 5.7 (SDAC Weekly Event Summary).

56
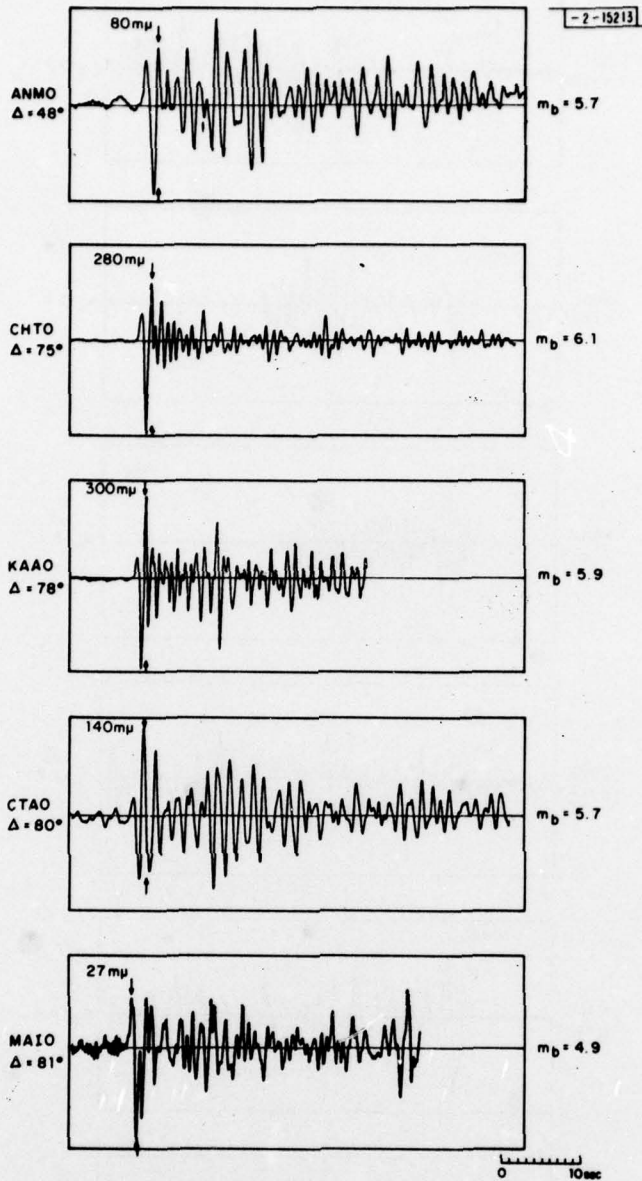
Fig. III-5. Event parameters. Region: Fox Islands; date: 23 November 1977; origin time: 16:55:22; location: 51.94°N, 171.43°W; depth: 57 km, m_b = 5.5 (SDAC Weekly Event Summary).

57
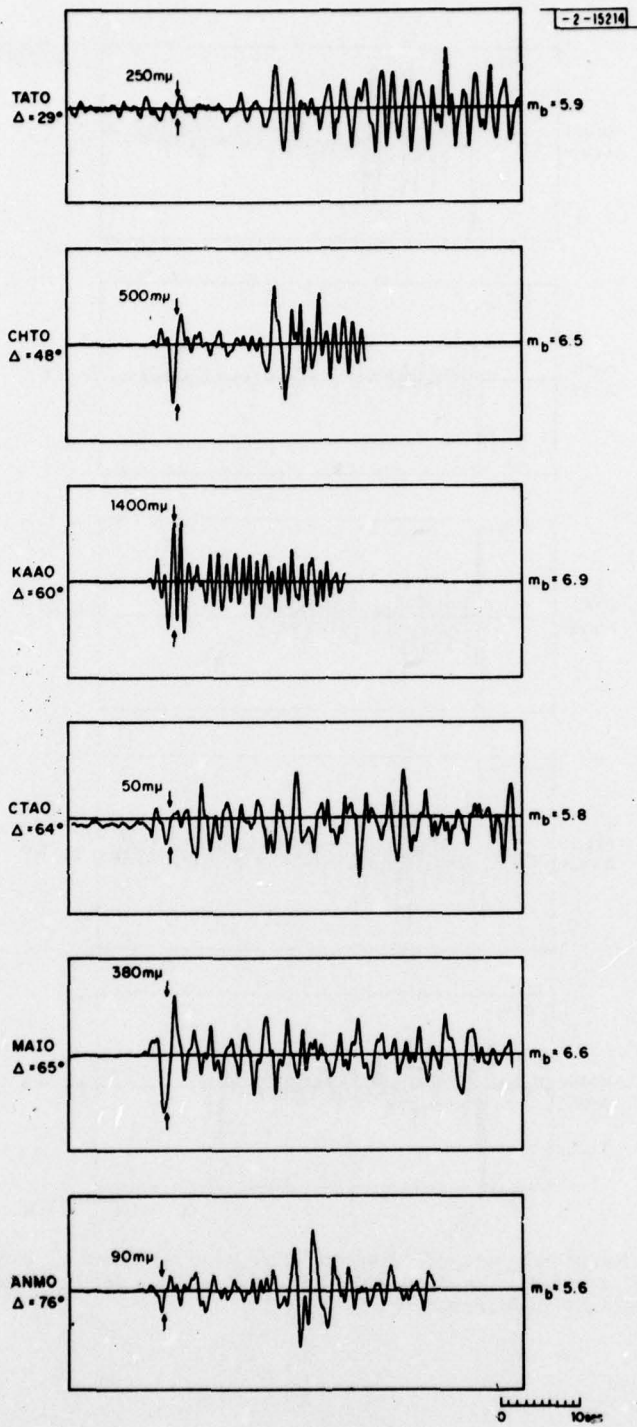
Fig. III-6. Event parameters. Region: Kuril Islands; date: 22 March 1978; origin time: 0:50:35; location: 43.84°N, 148.91°E; depth: 47 km, m_b = 6.1 (SDAC Weekly Event Summary).

58
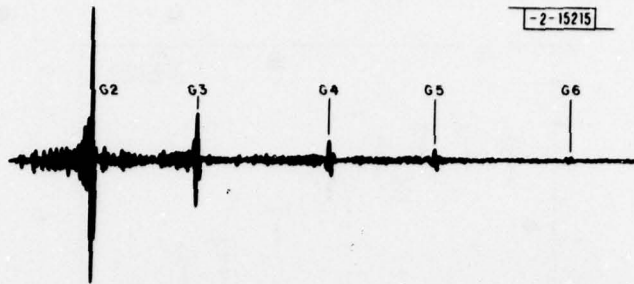
Fig. III-7. Low-pass filtered transverse component recording at SNZO of earthquake in southwest Atlantic Ocean. Seismogram starts 4000 sec after origin time, is ~7 hr in duration. Love waves G2 through G6 shown.
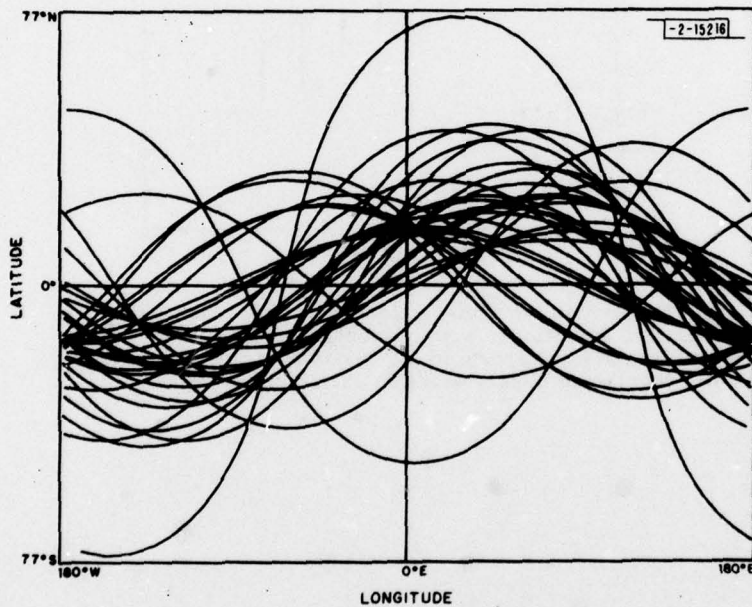
Fig. III-8. Circumferential paths for event-station pairs given in Table III-2 (mercator projection). Sampling is more dense for Southern Asia, Northern Africa, South America, and the Southern Pacific. More-uniform sampling will be obtained by an extension of this study.
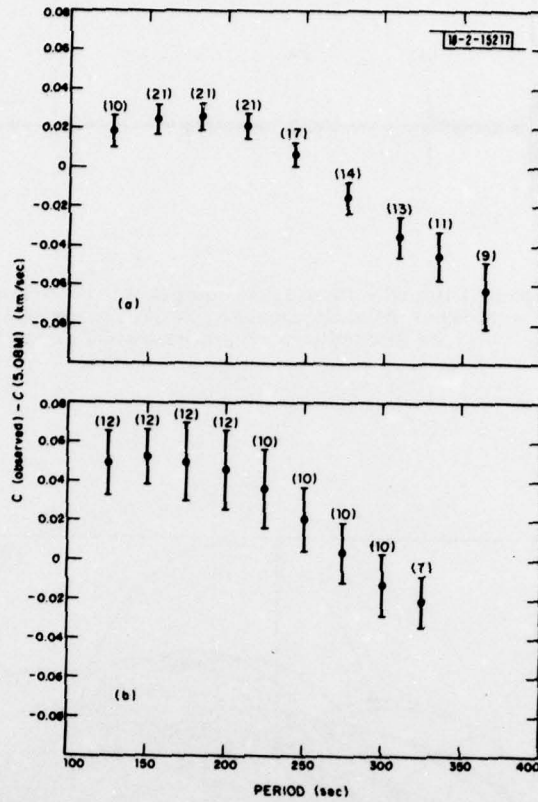
Fig. III-9. Love-wave phase velocities, expressed as means and standard deviations, with respect to model 5.08M (Ref. 9). Present results are shown in (a), those of a previous study[10] in (b). Number of observations at each datum is given.
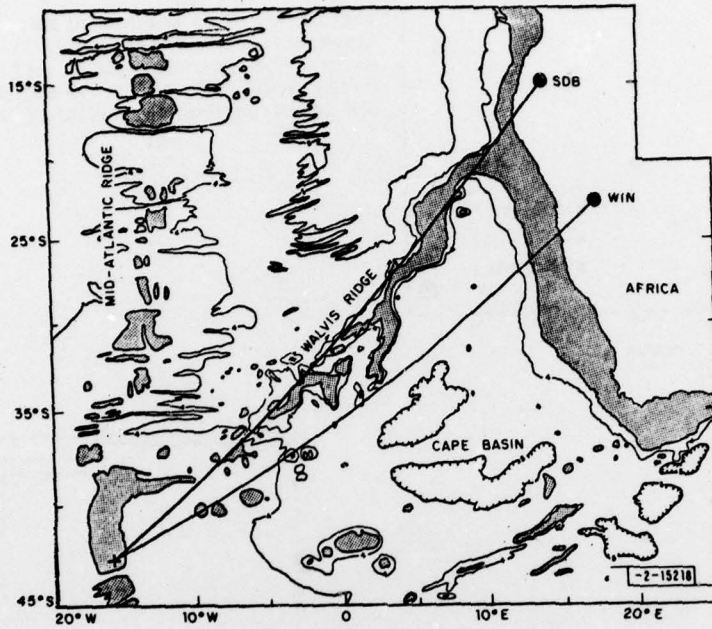
Fig. III-10. Index bathymetry chart of South Atlantic Ocean showing Walvis
ridge extending southwestward from African margin to mid-Atlantic ridge.
Depths contours are in thousands of meters. Depths shallower than 3000 m
are stippled. Curved arcs show ray paths between mid-Atlantic ridge earth-
quake epicenters (cross) and WWSSN stations SDB and WIN.
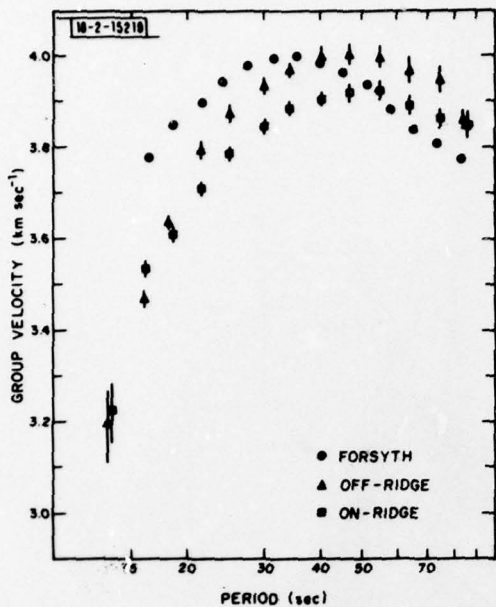
Fig. III-11. Comparison of Rayleigh-wave dispersion curves derived from inversion method for on-ridge (SDB) and off-ridge (WIN) paths with 20- to 50-million-year-old crust pure-path results of Forsyth.[19]

Fig. III-12. Comparison of shear-wave velocity profiles for on-ridge and off-ridge models with Forsyth[19] pure-path model.
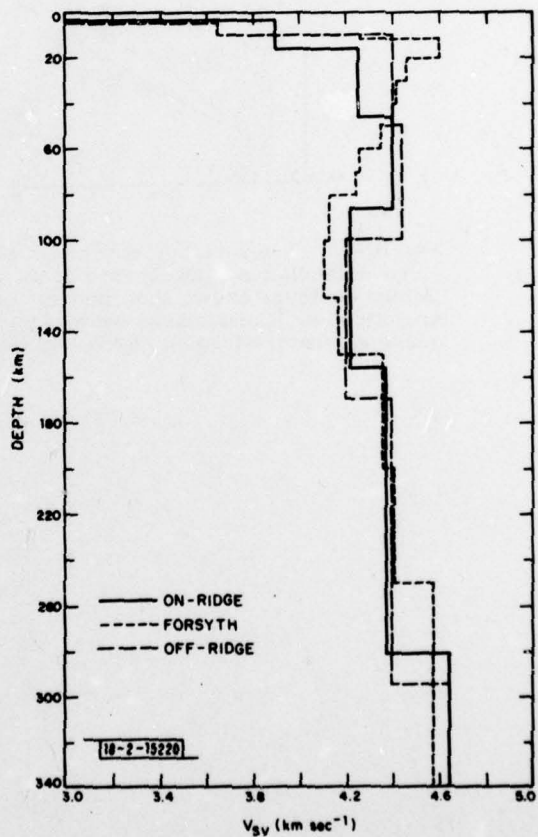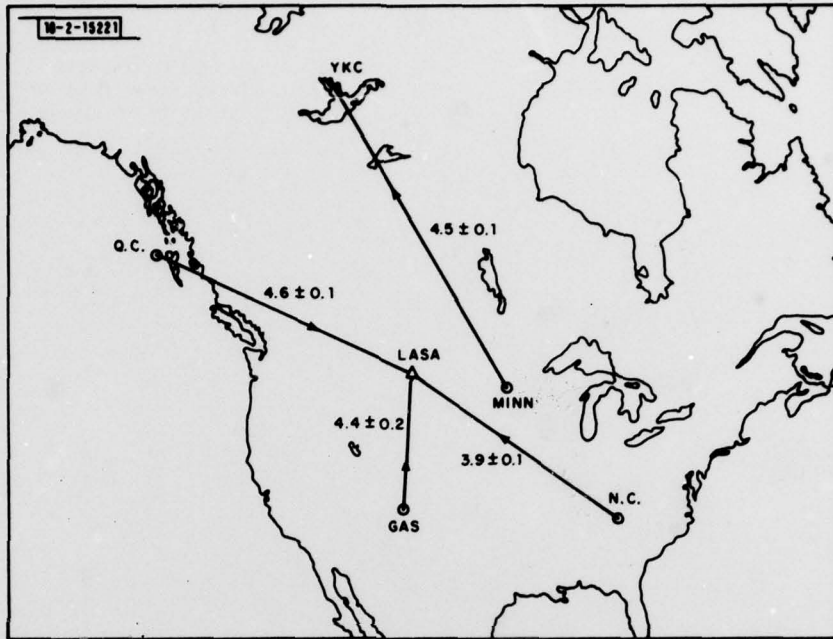
Fig. III-13.   Phase velocity of vertical component of L_g at group velocity
3.5 km/sec at 1 Hz.

IV. COMPUTER SYSTEMS AND DATA COLLECTION

A. A UNIX DATA-ANALYSIS AND DISPLAY SYSTEM

The imminent demise of the PDP-7 computer systems necessitates the transfer of a number of software packages from the PDP-7 system to UNIX. One of the most notable of these is the Data Analysis and Display System (DADS). The following section is a brief description of a version of the DADS that we currently are designing for UNIX.

1. General Description

The UNIX DADS is a data-management system designed specifically for seismic databases. The system is general enough to store the large variety of data and data types needed in seismic databases. It is also specific enough to take advantage of some of the efficiencies made possible by the basic properties of seismic databases. DADS makes no claim at being a general data-management system.

Conceptually, DADS may be thought of as a two-dimensional data matrix. Matrix rows represent data objects whose properties are stored in the database. Each matrix set of values is used to delineate the properties of the data objects. Each matrix column is defined as having an explicit data type such as time, depth, or magnitude.

A typical DADS data matrix is a seismic event list. Each row in the event list represents some seismic event. The columns represent the properties of the events such as depth, time, and magnitude. Columns may also be used to represent larger entities such as lists of arrival times for each event, or even a list of waveforms for that event.

There are a variety of commands which may be used to manipulate DADS databases. A command line interpreter accepts a set of DADS commands and executes them. These commands specify subsets or supersets of databases and what is to be done with them. The user may wish to search the database for a particular subset of data and store it in a new database.

Other operations of interest are the "table" command, which allows users to display the specified data set in table form, a graph command, which allows the user to plot two variables, and a set of commands to perform arithmetic calculations.

2. Implementation: File Structure

The DADS implementation relies on a number of fundamental assumptions. The most-important assumption is that most of the computation done by the DADS software will be in the form of database searches. The amount of processing needed to generate a new textual display of a database is negligible compared with the processing required for database searches. Another assumption is the type of terminals which will be used as DADS consoles. DADS is designed to work well with Tektronix 4014 and VT52 terminals. It does not work with Decwriters or any other hardcopy terminals.

The file structure used to implement DADS reflects the efficiency considerations mentioned above. Each database is a file directory which contains a collection of files of three types. The first file type is the header file which contains a description of the database or database subset, along with bookkeeping information. The second file type is the data file which is used to store database data. The last file type is the selector file that contains the information used to select which portions of the data belong to which database subsets.

65

Header Files

	master header file	subset 1 header file	subset 2 header file

512 character buffer for database ID

selector

	00	01	10

Data columns and their data types

	master		subset 1		subset 2	
1	depth integer	1	depth integer	1	time long
2	magnitude integer	2	magnitude integer	2	longitude float
3	date long	3	date long	3	latitude float
4	latitude float					
	longitude float					
	waveforms filename					

Data Files

512 character ID

data selection for each event

	selector file	depth in meters	date		waveform
1	00	depth 1	date 1		wave.1.g
2	10	depth 2	date 2		wave.2.g
3	10	depth 3	date 3	...	wave.3.g
4	10	depth 4	date 4		wave.4.g
5	11	depth 5	date 5		wave.5.g
6	11	depth 6	date 6		wave.6.g
7	01	depth 7	date 7		wave.7.g
8	10	depth 8	date 8		wave.8.g

Fig. IV-1. Sample database (for explanation, see text).

The data files are organized by data matrix column. Each data file is a one-dimensional array whose elements delineate the data objects in the database. The constituent data elements of a data object are the elements with the same index within each data file specified by the header file. This configuration of data files has a number of advantages for processing the data. A search or scan of the values of one data descriptor is reduced to a sequential scan of one data file. The addition or deletion of a data column involves the simple addition or deletion of a file to the database. New entries in the database are implemented by appending a new data element onto each data file.

The header files along with the data selector file are the key parts of the database used to organize the data. The header file includes an identifying text string of up to 512 characters, a unique selector identifier (ID), and a set of data-type information for the data column files. There is one master header file which is used as an index of the entire database. The other header files are used to select database subsets. The master header file always has the same name as the database directory. The DADS is currently limited to 1 database master header file and 30 database subset header files.

The selector ID is used in conjunction with the selector file to identify which of the data objects belongs to a particular database subset. The selector file is a one-dimensional array similar to the data files. Each element in the array contains a key that identifies the database subsets to which the corresponding elements in the data files belong. The corresponding elements in the data files are those elements with the same file index as the selector file element. The selector ID itself is a long integer with one bit set to 1. Each database subset is assigned a different bit. A selector match occurs if the logical AND of the selector ID and the selector file element is nonzero. A scan of any database subset will therefore begin with a scan of the selector file to see if the data in any particular row are elements of that subset.

The data column information in a header file consists of a character string of up to 8 characters and an integer data type code. The 8 characters correspond to data file names in the database directory. The data type code corresponds to the legal data type codes such as integer, real float, etc. which may be found in a data file.

A sample database is shown in Fig. IV-1. The database is an event list with 7 data columns of varying data types. Also included are two database subset groupings of three data columns each. The selector file indicates which rows in the database correspond to which subsets of the database. In the example, 00 indicates that a row is only a member of the whole database and not in any subset. A 01 indicates that a row is a member of subset 1. A 10 indicates that a row is a member of subset 2. A 11 indicates that a row is a member of both subsets. The last column is a special data type. It contains the names of waveform files as elements.

3.   Implementation: Command-Line Interpreter

A simple interpretive language is used to access and manipulate DADS databases. The language has a limited syntax. It does not allow conditional, branch, or iteration statements. These features will be added at some future date. The language does allow the selection and manipulation of database subsets. It also interprets arithmetic expressions written in standard infix notation.

While any database in the system may be accessed with a command string, it is more efficient to specify the current database of interest. This may be done with the command line:

current events;

where "events" is the name of a database header file in the local database directory. The current database can be changed at any time. References which do not use the current database must include the relative pathname of that database. These references will be considerably less efficient. It is also recommended that the user move to the directory in which a database is located before invoking the DADS on that directory. The DADS is invoked with the shell command:

dads "databasename";

The manipulation of a database is accomplished through a combination of Boolean expressions and assignment statements. The Boolean expressions are used to select a subset of the database. The subset may include any number or combination of data matrix columns or rows. The method used for specifying rows is a comparison test. An example of this is the selection of a data subset from an event list database. If only those events between 1960 and 1970 with magnitude greater than 7 are to be selected, one would use the following Boolean expression:

magnitude > 7 && 1960 < year < 1970;

If only the depth, magnitude, and year data columns are required, one would expand the statement to:

magnitude > 7 && 1960 < year < 1970:depth, magnitude, year;

The target of this database subset could be either a stored database subset or a display of the data. A stored subset may be created by declaring a subset database header variable and assigning it the result of the Boolean expression:

subset foo;
foo = magnitude > 7 && 1960 < year < 1970:depth, magnitude, year;

The database or database subset is displayed with the "table" command. This command acts as a function call and can be used with either a database name or a Boolean expression as a parameter. Two examples of this are:

table(foo);
table(magnitude > 7 && 1960 < year < 1970:depth, magnitude, year);

In the first example, the database with name foo is displayed. In the second example, the subset of the current database as specified by the Boolean expression is displayed. "Table" can also work on individual data columns within a database. The command:

table(:year);

is also legal if year is a database column. In this case, one entire database column (or as much as will fit on a screen) is displayed.

Individual database columns can also be manipulated through interpretive language. For example, the command lines:

column logdepth
logdepth = log(depth);

define a new data column logdepth in the current database and store the log of all the corresponding entries of the depth column. The data type of logdepth will be coerced to the same data type

as the depth column. It is also possible to specify columns from a database other than the current one. This is done by specifying the relative pathname to each data column involved. For example, the command line:

../events/logdepth[1] = log(depth[1]);

assigns the log of the first entry of the "depth" column in the current database to the third entry in the "logdepth" column which is located in the "events" database. The events database is a sibling of the current directory. This command line also demonstrates how individual elements within a data column can be accessed.

The arithmetic expressions allowed by the interpretive language include the standard operators such as + - * / as well as Boolean operators and certain function operators. The user may declare variables in any legal database datatype and use these variables in the arithmetic expressions. Data columns and database header file names are permissible data types for certain types of arithmetic expressions.

<div align="right">J. Sax</div>

B. UNIX SIGNAL DISPLAY PACKAGE

During the past six months, we have made three significant improvements in the UNIX Signal Display Package.[†]

First, a cursor feature has been implemented. The user can now call up the Tektronix cursor and use it to set named markers which visually flag particular data points of a seismogram. The locations of these markers become a permanent part of the database and may be used as input to related seismic-processing programs.

Second, the Display program has been modified to utilize the Versatek capability of our graphics software. There are two options: the user may choose to get a Versatek copy of the current picture on his screen, or he may choose to extend the waveforms off to the right for a maximum output of 9 Versatek pages (76 in.).

Third, the speed of the Display program has been increased substantially by eliminating options that were no longer needed and improving the efficiency of certain I/O operations.

<div align="right">L. J. Turek</div>

C. TEKTRONIX GRAPHICS SPEEDUP

The UNIX graphics system is currently too slow to be used as a truly interactive system. Although there are many contributing factors to this problem, one of the major problem areas is the communication link between the PDP-11 processor and the Tektronix graphics terminal. This link currently consists of a standard 9600-baud teletype interface. Analysis of the system software and hardware indicates that this communication link is too slow to effectively service the Tektronix 4014 terminal.

The system software is particularly inefficient in the way it handles character device interfaces. While the interface is acceptable for normal teletype usage, the software overhead of handling character buffers is particularly painful. The character device interface was not designed to handle the large volume of data required to transmit a graphics picture to the Tektronix.

[†] Seismic Discrimination Semiannual Technical Summary, Lincoln Laboratory, M.I.T. (31 March 1978), DDC AD-A057279.

The hardware also contributes to the problem. The Tektronix 4014 is capable of accepting graphics characters at rates approaching 50K baud rather than the 9600 baud provided by the teletype controller. The increased data rate can be achieved by synchronizing the data flow from the CPU with the rate at which the Tektronix screen is painted. The synchronization is necessary because the rate at which a Tektronix can accept data varies with the rate at which it draws vectors. The vector drawing rate, in turn, varies with the size of the vectors.

A properly designed interface between the PDP-11 and the Tektronix terminal should go a long way toward speeding up graphics. The design must include both software and hardware modifications to the PDP-11 to Tektronix interface. The software character handling overhead must be eliminated, and hardware data synchronization mechanism must be developed.

1. Interface Hardware

The hardware configuration of the graphics interface consists of a DMA I/O device at the CPU end, and a parallel interface with synchronization control at the Tektronix terminal. The DMA device has a software interface similar to the DEC DR11-b. Its command and status registers will perform basically the same functions as the DR11-b. In addition, the DMA device has a FIFO buffer of about 512 bytes. The FIFO is used to store data waiting to be transferred to the Tektronix.

The Tektronix interface is the general-purpose parallel interface 021-0109-00. It has the necessary control logic to handle up to 8 separate terminals. Each terminal has a separate address which the CPU specifies when transmitting data to a terminal.

2. Interface Software

The interface software treats the DMA device as a block I/O device rather than a character I/O device. This allows for the efficient transfer of up to 512 bytes directly from memory. While these block transfers are somewhat wasteful for normal teletype interactions with the Tektronix terminal, they are absolutely essential for efficient data transfer of graphics data.

The user program interface to the Tektronix terminals is totally unaffected by the software and hardware modifications.

3. Data Transfers

A data transfer from the CPU to the terminal begins with a DMA transfer of a block of data from memory to the FIFO. This causes a data-ready flag to be raised on the Tektronix interface. The first byte of the data specifies which terminal is to receive the data. The specified terminal gains control of the Tektronix data interface. The terminal initiates a data transfer by strobing the FIFO register for each byte of data to be transmitted. The strobe rate is governed by the rate at which the data can be executed as graphics commands by the terminal. The DMA resets the data-ready line after the last byte in the FIFO has been transmitted to the Tektronix. The DMA interface also generates an interrupt to the CPU to indicate that the data transfer is complete. The CPU may now send the next data block to the FIFO for transmission to a Tektronix terminal.

A timeout mechanism is included in the DMA device for measuring the response time of a Tektronix terminal. If the terminal does not respond within 1 sec to a data-ready line or if the time between data strobe pulses exceeds 1 sec, the terminal is declared down, the FIFO will be

flushed, and an error interrupt is sent to the CPU to indicate a failure in the data transmission. This mechanism will prevent a dead terminal from tying up the graphics interface.

Data transmission from a Tektronix terminal to the CPU is initiated by the terminal, which sends an interrupt on one of 8 lines to the DMA device. Upon receiving an interrupt, the DMA device strobes the appropriate terminal to transmit the data to PDP-11 memory via the DMA input registers.

The overall interface design is relatively simple and could be completed with only a modest investment in hardware and software design and implementation. The only significant difficulty will be in building the DMA device for the PDP-11. Standard DMA interfaces built by DEC or other manufacturers do not include all the control logic necessary for this particular interface. One possible starting point is the MDB11-b general-purpose DMA controller which provides a generalized DMA interface for the PDP-11 UNIBUS, including the necessary control and status registers. This device can be used in conjunction with the MDB11-ww wirewrap expansion module which is needed to hold the additional circuitry for the FIFO and the control logic to be used in conjunction with the Tektronix interface. The entire package makes possible a significant speedup of the Tektronix graphics.

<div align="right">J. Sax</div>

D. DATACOMPUTER SOFTWARE

Access to the SRO raw data files has been improved. In the 31 March 1978 SATS, we described a new program (called DCRISP) which outputs properly formatted Datacomputer short-period (SP) request files by computing the theoretical arrivals at SRO stations for an input event list. We have rounded out this project by adding a second program (called DCRILP) which performs the same function for long-period (LP) arrivals.

We have also added a new program, called WFDAY, which will access the Preliminary Summary Waveform Files that are now being created. These are files that will eventually contain all the waveform segments associated with a given event. SRO data are not yet being stored in these files, but data from certain Alaskan stations are stored in these files and nowhere else.

WFDAY has two modes of operation: it will either retrieve all the waveform segments for a given day, or it will retrieve all the waveform segments stored for a specified event. The resulting data will be reformatted and stored in a UNIX waveform database, ready for viewing with the Display program, etc.

<div align="right">L. J. Turek</div>

E. TAPE DATA COLLECTION

Until recently, the Applied Seismology Group has housed a library of nearly 12,000 digital tape reels of data from LASA, NORSAR, and ALPA. It has not been possible to carry out adequate tape maintenance on a collection of this size. As a result, the earlier portions of data have been subject to deterioration. Specific problems noted have included surface deformations and shedding of the oxide coating, which result in extensive data dropouts, and some complete voids.

As a result of these problems, and the fact that use of these data has decreased substantially in the last few years, we have decided to make a significant reduction in the size of the data collection. With the exception of data for underground explosions, all LASA data for the period 1965 through 1969 are being removed from the library, as are all reels containing noise and other special-purpose information. Approximately 5000 of these tape reels contain useful

<div align="center">71</div>

information. We hope to identify an archiving agency which will assume the storage and maintenance of these tapes.

The collection which we will maintain consists of LASA, NORSAR, and ALPA data for the years 1970 through 1973, plus the explosion-data set. This collection will number just over 3000 tape reels. The maintenance program will consist of respooling and cleaning the tapes every year, and transferral to new tapes every 10 years.

The array data collection is now being supplemented by the network day tapes from the SRO network, which are being received on a regular basis.

L. E. Sargent

GLOSSARY

ALPA	Alaskan Long Period Array
ASRO	Upgraded High-Gain Long-Period Station
CLVD	Compensated Linear Vector Dipole
CPU	Control and Processing Unit
DADS	Data Analysis and Display System
DEC	Digital Equipment Corporation
DMA	Direct Memory Access
FIFO	First In, First Out
ISC	International Seismological Center
J-B	Jeffreys-Bullen (Tables)
LASA	Large Aperture Seismic Array
LP	Long Period
NORSAR	Norwegian Seismic Array
NTS	Nevada Test Site
ORM	Ocean Ridge Velocity Model
PDE	Preliminary Determination of Epicenters
SATS	Semiannual Technical Summary (Report)
SDAC	Seismic Data Analysis Center
S/N	Signal-to-Noise Ratio
SP	Short Period
SRO	Seismic Research Observatory
WWSSN	World-Wide Standard Seismograph Network

REPORT DOCUMENTATION PAGE		READ INSTRUCTIONS BEFORE COMPLETING FORM
1. REPORT NUMBER ESD-TR-78-259	2. GOVT ACCESSION NO.	3. RECIPIENT'S CATALOG NUMBER
4. TITLE (and Subtitle) Seismic Discrimination		5. TYPE OF REPORT & PERIOD COVERED Semiannual Technical Summary 1 April – 30 September 1978
		6. PERFORMING ORG. REPORT NUMBER
7. AUTHOR(s) Michael A. Chinnery		8. CONTRACT OR GRANT NUMBER(s) F19628-78-C-0002
9. PERFORMING ORGANIZATION NAME AND ADDRESS Lincoln Laboratory, M.I.T. P.O. Box 73 Lexington, MA 02173		10. PROGRAM ELEMENTS, PROJECT, TASK AREA & WORK UNIT NUMBERS ARPA Order 512 Program Element No. 62701E Project No. 8F10
11. CONTROLLING OFFICE NAME AND ADDRESS Defense Advanced Research Projects Agency 1400 Wilson Boulevard Arlington, VA 22209		12. REPORT DATE 30 September 1978
		13. NUMBER OF PAGES 82
14. MONITORING AGENCY NAME & ADDRESS (if different from Controlling Office) Electronic Systems Division Hanscom AFB Bedford, MA 01731		15. SECURITY CLASS. (of this report) Unclassified
		15a. DECLASSIFICATION DOWNGRADING SCHEDULE

16. DISTRIBUTION STATEMENT (of this Report)

Approved for public release; distribution unlimited.

17. DISTRIBUTION STATEMENT (of the abstract entered in Block 20, if different from Report)

18. SUPPLEMENTARY NOTES

None

19. KEY WORDS (Continue on reverse side if necessary and identify by block number)

seismic discrimination	surface waves	NORSAR
seismic array	body waves	ARPANET
seismology	LASA	

20. ABSTRACT (Continue on reverse side if necessary and identify by block number)

This report describes 20 investigations in the fields of seismic discrimination and the analysis of data from a global seismic network. These are grouped as follows: the estimation of event location and focal depth (4 contributions), the estimation of the source moment tensor (5 contributions), miscellaneous studies (6 contributions), and computer systems and data collection (5 contributions).

DD FORM 1473 EDITION OF 1 NOV 65 IS OBSOLETE
1 JAN 73